



Propulsion effects after laser ablation in water, confined by different geometries

Matej Senegačnik¹ · Matija Jezeršek¹ · Peter Gregorčič¹

Received: 15 October 2019 / Accepted: 10 January 2020
© Springer-Verlag GmbH Germany, part of Springer Nature 2020

Abstract

A Nd:YAG laser with 7-ns pulses and pulse energies up to 10 mJ is used to induce an optical breakdown in the front surface of an aluminum rod, covered by a water layer. The rod is part of a ballistic pendulum. In this way, we study the propulsion effects by means of coupling coefficient and energy-conversion efficiency with respect to different confining geometries, volumes of water applied to the front surface of the rod, and the distance of this surface from the laser-beam focus. Holes with different dimensions are drilled on the target surface and filled with different volumes of water to examine the influence of the confinement by the liquid (a free boundary) and a solid-surface geometry on laser ablation effects. The rod movement and the water ejection after laser ablation are acquired by a high-speed camera with 10k frames per second. The results show that the confinement by cavity substantially increases the propulsion effects by shaping the ejected flow of the liquid; while the cavitation bubble, induced inside the water layer, plays a significant role in propulsion efficiency. From the presented results, it follows that the laser-propelled rod carries below 0.5% of the total mechanical energy after propulsion, while the rest of this energy represents the kinetic energy of the ablated water. As expected, moving the target surface away from the focal position decreases the ablative-propulsion efficiency. When the focus is moved inside the solid target, the decrease occurs due to lower conversion of the pulse energy into the energy of the cavitation bubble. If the focus is moved from the surface outward, the bubble moves towards the liquid–gas interface and it is not able to efficiently eject all the liquid from the target.

Keywords Laser ablation · Laser propulsion · Cavitation bubble · Nanosecond laser · Coupling coefficient · Energy-conversion efficiency

1 Introduction

Interaction between laser light and a solid (reflective and/or absorbing) object always results in increased linear momentum of the irradiated object that manifests as propulsion [1], due to material recoil [2] and/or radiation pressure [3]. In case of pure-radiation pressure, the totally reflective object gains the momentum $p = 2E_p/c$, where E_p stands for pulse energy and c is the speed of light. For a pulse energy of 10 mJ, this momentum equals $\sim 7 \times 10^{-12}$ Ns. However,

pure-photon pressure is limited by the threshold fluence for laser ablation. If this fluence is exceeded, the material is ablated and the gained momentum is approximately three or four orders of magnitude higher than in the case of pure-radiation propulsion. The force impulse can be significantly increased, if the irradiated surface is confined by a liquid or other layer [4]. In this case, the confinement geometry, defined by the thickness of the liquid layer [5, 6] and/or by the geometry of the solid surface [7], plays a significant role [8].

The propulsion effects are most commonly quantified by the coupling coefficient and the energy-conversion efficiency. The coupling coefficient C_m is defined [9] as the ratio between the gained momentum and the laser pulse energy E_p as:

$$C_m = \frac{mv}{E_p}. \quad (1)$$

Electronic supplementary material The online version of this article (<https://doi.org/10.1007/s00339-020-3309-y>) contains supplementary material, which is available to authorized users.

✉ Peter Gregorčič
peter.gregorcic@fs.uni-lj.si

¹ Faculty of Mechanical Engineering, University of Ljubljana, Aškerčeva 6, 1000 Ljubljana, Slovenia

It represents the figure of merit for the interaction between a laser pulse that is incident on the target surface [10]. In Eq. (1), m stands for the mass of the propelled object, while v is the amplitude of the gained velocity.

On the other hand, the energy-conversion efficiency η that is defined as the ratio between the gained kinetic energy of the propellant and the pulse energy quantifies the share of the optical energy that is converted into mechanical motion [11, 12]:

$$\eta = \frac{mv_0^2}{2E_p}. \quad (2)$$

The aim of this work is to study the propulsion effects during pulsed laser ablation in liquids [13] that is important for diversity of applications, including nanoparticle generation [14, 15], laser-induced forward transfer [16, 17], laser shock peening [18–20] and different laser medical applications [21–23]. The propulsion effects are investigated for different shapes of a blind hole filled with different volumes of water. To measure the gained momentum and the mechanical energy, the blind holes are drilled into the front surface of an aluminum rod that is part of a ballistic pendulum. The ablated water and the propelled rod are observed using a high-speed camera. The optical energy of laser radiation is transferred into the mechanical energy of the ablated liquid and the mechanical energy of the propelled solid. Using the conservation of linear momentum, we estimate the share of the mechanical energy, carried by the propelled solid, since this part of the mechanical energy is particularly important for laser propulsion [24, 25].

2 Experimental setup

To study the effects on ablative laser propulsion, we used a Nd:YAG laser emitting 7-ns pulses with 1064-nm wavelength. Pulse energy was varied between $E_1 = 10.6$ mJ and $E_2 = 5.3$ mJ. Laser irradiation was firstly reflected by a dichroic mirror and then focused by a lens with a 100-mm focal length. Finally, it was reflected by an additional mirror on the target surface, as sketched in Fig. 1.

As a target, we used an aluminum rod with a 4-mm diameter, 68-mm length and approximately $m_R = 2.4$ g mass. The mass was determined using a precise scale Shimadzu AX 200. A camera with a CMOS sensor was positioned above the dichroic mirror for the purpose of positioning the center of the target surface in the irradiation spot, as well as maintaining a constant distance from the focus during the measurement repetitions. The position of the irradiation spot on the target surface during the repetitions was varied (at a constant distance from focus) in the area approximately 200 μm around the center of the rod, to mitigate the formation of a narrow indentation due to material ablation.

To increase the gained momentum of the rod after ablation, different volumes of distilled water were applied to the target surface, while three different geometries of the target surface were used, as depicted in Fig. 2. Experiments were performed on a flat surface (F) as well as on a surface with 2-mm (D2) and 3-mm (D3) wide cylindrical blind holes. The geometries of the rods after the experiments have been analyzed with a 3D optical confocal microscope Alicona InfiniteFocus to extract the 3-dimensional models, and the depth profiles across the rod's axis as well as to determine

Fig. 1 Experimental system

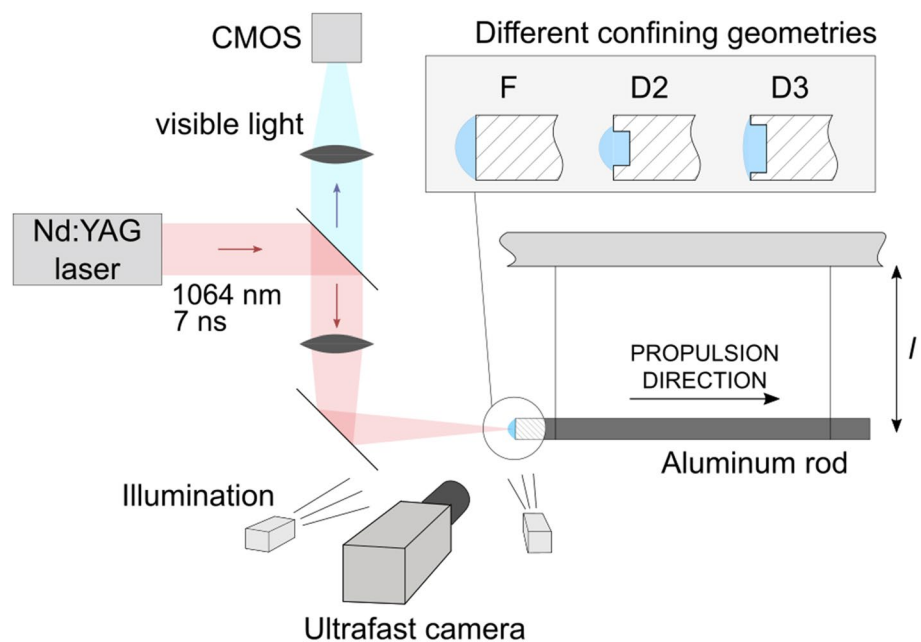
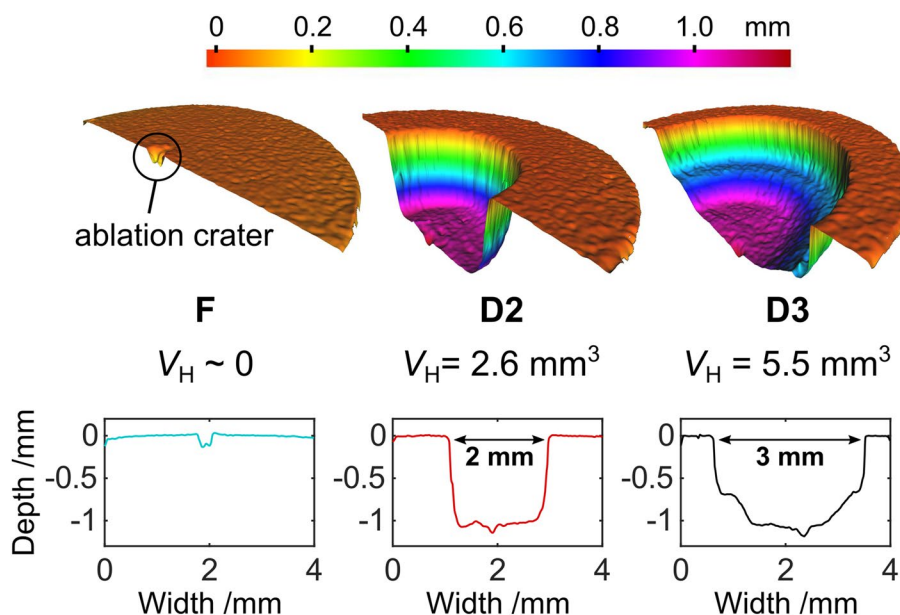


Fig. 2 Different geometries of the rod’s target surface used in the experiments. Bottom graphs present the corresponding 2D depth profiles across the rod’s axis



the volume of the blind holes (indicated in Fig. 2 by V_H). Small craters in the center of the target surface are caused by material ablation during the experiments. The volume of the ablated material on the flat geometry was approximately 0.01 mm^3 after 50 experiments had been carried out with different parameters on that same surface.

At all the geometries (F, D1, D2), the experiments were performed at three different volumes of the distilled water (4 mm^3 , 6 mm^3 and 10 mm^3). The water was placed on the target surface of the rod using a calibrated pipet.

To measure the momentum, gained after the confined ablation, the rod was part of a ballistic pendulum, where the string length equaled $l = 117 \text{ mm}$ (Fig. 1). The pendulum movement was measured using a high-speed camera Photron Fastcam SA-Z type 2100K-M-64GB at 10,000 frames per second. Movement of the propelled aluminum rod was further tracked in Matlab using the cross-correlation of images acquired at different times during the pendulum oscillation. A black band at the front end of the rod was utilized for more consistent tracking. Tracking was also repeated several times for the same experiment with different masks and tracking points to minimize the image-processing error.

A harmonic function in the following form was fitted to the measured displacement of the rod Δx as a function of time t :

$$\Delta x(t) = A \sin(\omega t + \varphi_0) + x_0, \tag{3}$$

where A , ω , φ_0 and x_0 represent the fitting parameters of oscillation amplitude, angular velocity, phase shift and lateral shift, respectively. The amplitude of the linear velocity v_0 of the propelled rod can be extracted from the fitted parameters A and ω as:

$$v_0 = A\omega. \tag{4}$$

An example of the measured and the fitted lateral displacement of the pendulum after a laser ablation is shown in Fig. 3. For the selected points on the graph (Fig. 3a), the acquired images of the rod are presented in Fig. 3b–f.

2.1 Accuracy of the rod-movement tracking

The accuracy of the rod tracking was estimated by comparing the measured oscillation periods with the theoretical values, which can easily be determined from the physical models of the mathematical and the physical oscillators.

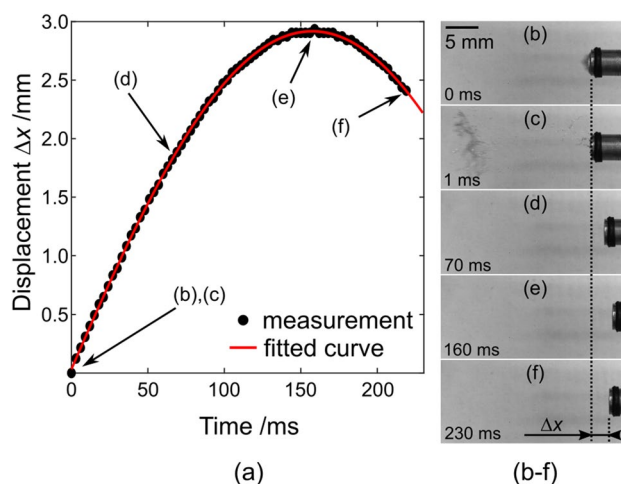


Fig. 3 Tracking of aluminum rod movement by ultrafast imaging: a measured displacement with the corresponding fitting curve (Eq. 3), b–f the images of the rod for the selected measured points in (a)

The key to accurate tracking of the rod is characterizing the translation of the rod with sufficient numbers of pixels. This ensures an accurate fit with narrower window of free parameters. Comparing the measured oscillation times with the theoretical values, a sufficient number of pixels per amplitude of oscillation were determined to be at around 50 px/A. When the maximum lateral displacement (amplitude) of the propelled rod in the acquired video equaled less than 50 pixels, the tracking proved difficult, which can be seen from the increased deviations in the measured oscillation times (Fig. 4).

A higher optical magnification should, therefore, be used for studying smaller displacements (induced by low pulse energies, fluences or volumes of water) to ensure an accurate

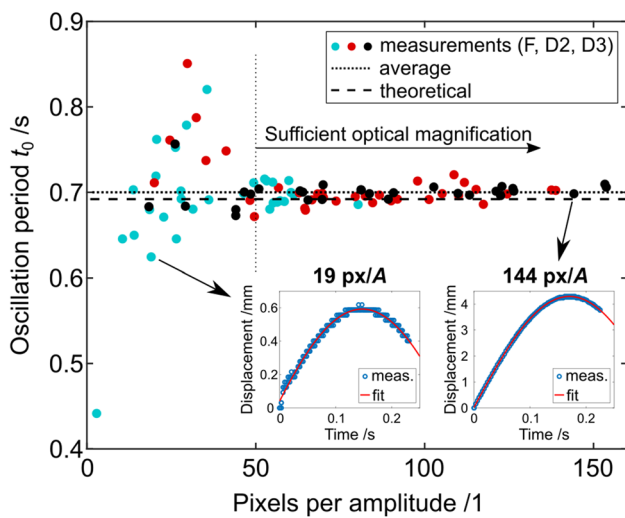


Fig. 4 Oscillation periods t_0 , obtained in the experiments with various parameters as a function of the amplitude A (in pixels). The larger oscillation amplitudes ensure a narrower window of free parameters, leading to more accurate measurements. The dotted line shows an average of all the measured values, while the theoretical value for a mathematical pendulum is shown by the dashed line

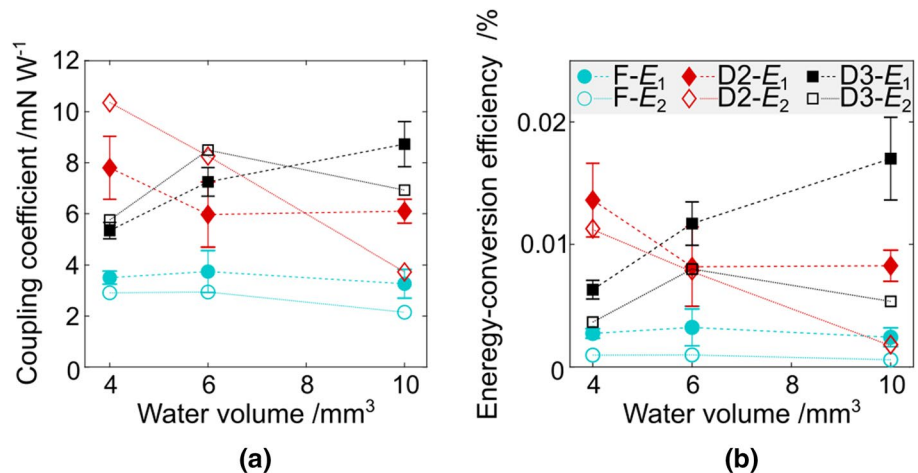
fit. However, in our case, all the experiments were performed with the same optical magnification that equaled 31 $\mu\text{m}/\text{px}$ to observe the flow of the ejected water at the same size and magnification. Thus, special care was taken and an increased number of fitting repetitions were utilized when fitting the experiments with smaller displacements to ensure comparable results.

Oscillation periods of all the used rods (F, D2, and D3) were calculated from the fitting parameter ω as $t_0 = 2\pi/\omega$. As visible from Fig. 4, they compare well to the theoretical period of a mathematical oscillator (the dashed line in Fig. 4). When accounting for mass distribution of the rod by incorporating a model of a physical oscillator, the theoretical period for our case is increased by around 1%, explaining the slightly larger experimentally measured average value (the dotted line in Fig. 4).

3 Results and discussion

The coupling coefficient as well as the energy-conversion efficiency was investigated at different parameters, including pulse energy, volume of water, confining geometry of the propelled aluminum rod, and ablation at different distances from focus. As visible from the results in Fig. 5, both—the coupling coefficient and the energy-conversion efficiency—are increased when the water is confined by a blind hole (geometries D2 and D3) compared to ablation confinement only by water applied to a flat surface (geometry F). Similar observations were reported by Zheng et al. when comparing water-confined target, glass layer-confined target and cavity target [8]. Yabe et al. have also studied laser propulsion [26–28], showing that the coupling coefficient decreases with increasing irradiation intensity due to plasma shielding [28]. Similarly, they experimented with covering the target surface with flat overlays of acryl and water and observed

Fig. 5 **a** The coupling coefficient and **b** the energy-conversion efficiency for different confining geometries (F, D2, D3) and pulse energies ($E_1 = 10.6$ mJ—the full symbols and $E_2 = 5.3$ mJ—the empty symbols) as a function of volume of the water layer



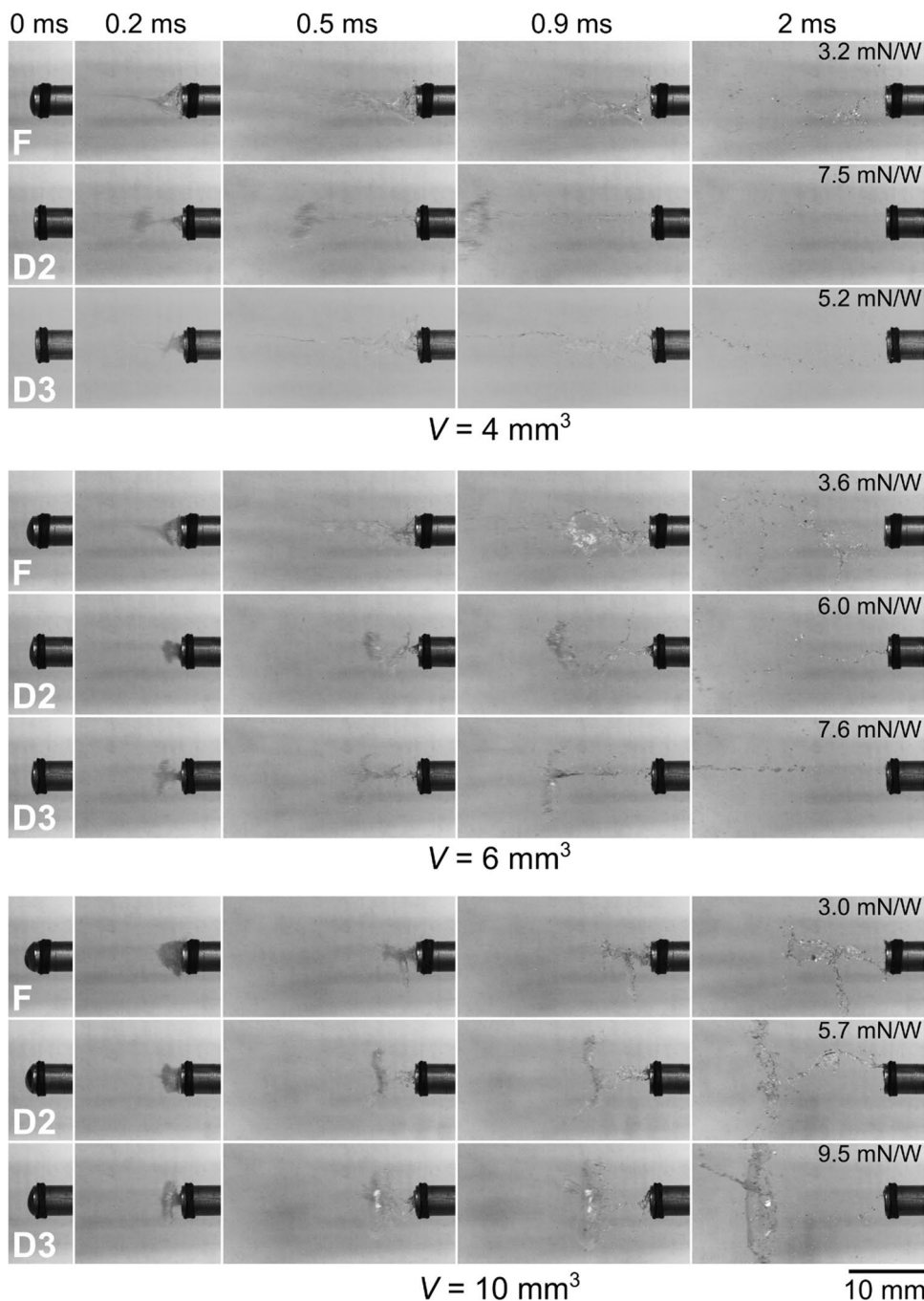
an increase in the coupling coefficient up to the values of 10 mN W^{-1} [29].

The quantitative results in Fig. 5 can be explained by typical sequences of images revealing the time evolution of the ejected water following the ablation (Fig. 6). In case of smaller volumes of water, a narrower hole (geometry D2 instead of D3) is favorable in terms of efficiency, as the ejected flow is directed in the outward direction with higher momentum. Only partially filling the blind hole with water ($V=4 \text{ mm}^3$, geometry D3) leads to very high

ejection velocities of the frontal water in form of a narrow jet. However, most of the remaining water follows with lower velocity, causing a decreased total momentum of the ejected material, since only smaller mass of water is ejected with high velocity. This lowers the overall momentum of propulsion.

Increasing the volume of water in case of a smaller blind hole (geometry D2) decreases the efficiency, as the ejected jet is not as uniformly directed. On the other hand, when the blind hole is larger (geometry D3), the increase in water

Fig. 6 The ejection of water following ablation confined by different geometries (F, D2 and D3, as shown in Fig. 2) for three different volumes of water (listed below each block of images). Laser is incident from the left; pulse energy equals 10.6 mJ. The coupling coefficient is noted in the top right corner of each row



volume is beneficial in terms of efficiency, since more water fits inside the hole, increasing the ejected mass.

The highest coupling coefficient and energy-conversion efficiency are achieved in combinations of narrow hole (geometry D2)—small droplet ($V = 4 \text{ mm}^3$) and wide hole (geometry D3)—large droplet ($V = 10 \text{ mm}^3$). In such situation, most of the applied water is ejected from the surface outward with similar velocity resembling a T shape, composing a flat front of liquid with little dispersion in the vertical direction. It should be noted here that the T shape refers to the shape of the cross section of the jet. The actual 3-dimensional shape of the jet is the letter T revolved around the central axis of the rod, since the phenomena are cylindrically symmetrical.

3.1 Distribution of the mechanical energy between the rod and the ablated water

The optical energy of the (several nanosecond long) laser pulse is converted into mechanical energy of the ejected water and the propelled rod through several successive mechanisms. As we discuss later, not all of them necessarily contribute to the final mechanical energy of the laser-propelled pendulum and the kinetic energy of the ablated water. In the first step, the plasma forms through an avalanche ionization in the focal position (after assumption that the water has no impurities) [30]. Since this plasma is a strong absorber of laser light, it results in a micro-explosion that drives a shock wave and a cavitation bubble [31, 32]. Further, the cavitation bubble dynamics results in a sequence of complex hydrodynamic processes [33] that are responsible for the liquid ejection and for a generation of a strong ultrasonic wave into the solid material (i.e., the front end of the rod) [6]. The aluminum rod may be considered as an elastic body. Thus, immediately after the ablation, the motion of this (elastic) rod is restricted to the mechanical wave that is much shorter compared to the length of the rod [1]. However, the mechanical wave reflects multiple times from the rod's front and rear sides. After each reflection, the dispersion widens the initially

short mechanical wave until its length becomes comparable to the length of the rod. In this way, the linear momentum of the ultrasonic wave is transferred to the whole body due to dispersion [34].

During the described processes, part of the optical energy of the laser pulse is converted into kinetic energy of water E_w as well as into kinetic energy of the rod E_R . The conservation of the linear momentum gives:

$$m_w v_w = m_R v_0. \quad (5)$$

Thus, by knowing the mass of the rod m_R and the mass of the ablated water m_w , the kinetic energy of water can be estimated from the measured amplitude of the rod's velocity v_0 as:

$$E_w = \frac{1}{2} \frac{m_R^2 v_0^2}{m_w}. \quad (6)$$

Considering that all the water is ablated, we have calculated E_w for different experimental parameters at the pulse energy $E_1 = 10.6 \text{ mJ}$. Table 1 lists the numerical values, including the total energy-conversion efficiency η_{tot} , defined as the ratio between the total mechanical energy and the pulse energy:

$$\eta_{\text{tot}} = \frac{E_w + E_R}{E_p}. \quad (7)$$

From the results in Table 1, it can be clearly seen that the majority of the mechanical energy—at the times, when the macroscopic motion of the whole rod is already observable—is carried by the ejected water and that the propelled rod in our case carries only up to 0.5% of the total mechanical energy (calculated from Table 1 as η/η_{tot}). Due to this reason, the measurements of the energy-conversion efficiency of the laser-propelled rod give significantly lower values compared to the energy-conversion efficiency of the laser ablation measured by other authors [11, 12]. However, when the total energy-conversion

Table 1 Measured rod velocity, v_0 ; amplitude of the propelled rod, A ; average coupling coefficient for the rod, C_m ; energy-conversion efficiency for the rod, η ; kinetic energy of the water, E_w ; and total energy-conversion efficiency, η_{tot} for the experiments with pulse energy $E_1 = 10.6 \text{ mJ}$ and front surface positioned in the focal spot

V/mm^3	Geom	$v_0/\text{mm s}^{-1}$	A/mm	$C_m/\text{mN W}^{-1}$	$\eta/\%$	E_w/mJ	$\eta_{\text{tot}}/\%$
4	F	15.6	1.8	3.5	0.003	0.17	1.7
4	D2	34.5	3.8	7.8	0.014	0.86	8.3
4	D3	23.6	2.6	5.3	0.006	0.40	3.9
6	F	16.6	1.8	3.7	0.003	0.13	1.3
6	D2	26.4	3.0	6.0	0.008	0.33	3.2
6	D3	32.1	3.6	7.2	0.012	0.49	4.8
10	F	14.5	1.6	3.3	0.002	0.06	0.6
10	D2	27.0	3.0	6.1	0.008	0.20	2.0
10	D3	38.7	4.3	8.7	0.017	0.43	4.2

efficiency, η_{tot} , is considered, our values are of the same order of the magnitude as values in Refs. [11, 12].

Although detailed energy balance of the conversion of light energy into mechanical energy is beyond the scope of this paper, the following can be reviewed from the existing literature. Before laser pulse reaches the target surface, portion of the pulse energy ($\sim 2\%$ in our case) is reflected from the air–water interface. If the target is placed 1 mm below the water surface, additional 6% of the rest of the pulse is absorbed in water, since the absorption coefficient of water for 1064 nm wavelength equals 60.6 m^{-1} [35]. In case of the nanosecond-laser pulses, the plasma forms when the pulse intensity reaches the threshold intensity [36]. Thus, some portion of the pulse energy is lost as absorption in (or reflection from) the target before plasma formation. Additional 5–6% of the pulse energy is required for the liquid evaporation within the plasma volume [37]. The rest of the energy is converted into mechanical energy of the cavitation bubble, the shock wave spreading into the liquid and the ultrasonic wave spreading inside the solid material. In case of laser pulses with similar parameters as in our study, Vogel et al. [37] reported for an infinite liquid (not confined by a solid body) that the bubble takes 20–25% of the pulse energy, while the shock wave carries 31–42% of the

pulse energy. Additionally, their results also suggest that within first 10 mm of propagation, approximately 85% of the shock wave energy is dissipated (assuming the sound speed in water this happens in approximately first $7 \mu\text{s}$ after the excitation-pulse irradiation). As shown in the next subsection, the mechanical energy of the laser-induced cavitation bubble in our case is measured to be up to 22% of the excitation pulse, which corresponds well with the values reviewed from the literature.

3.2 The evolution of the water ejection

Figure 7 shows the evolution of water ejection from the surface with flat geometry (F) when different volumes of water are applied. Here, the back-illumination is used for the high-speed imaging of the ejection to ensure better intensity and contrast of the acquired images. The rod was oriented vertically to avoid non-symmetry of the phenomenon due to gravity. Furthermore, the rod in this case was not part of a ballistic pendulum—its position was fixed.

As can be seen from the results in Fig. 7, the ejection begins by changing the shape of the water–air interface. This is a consequence of the cavitation bubble development which in our case cannot be seen due to the curved water

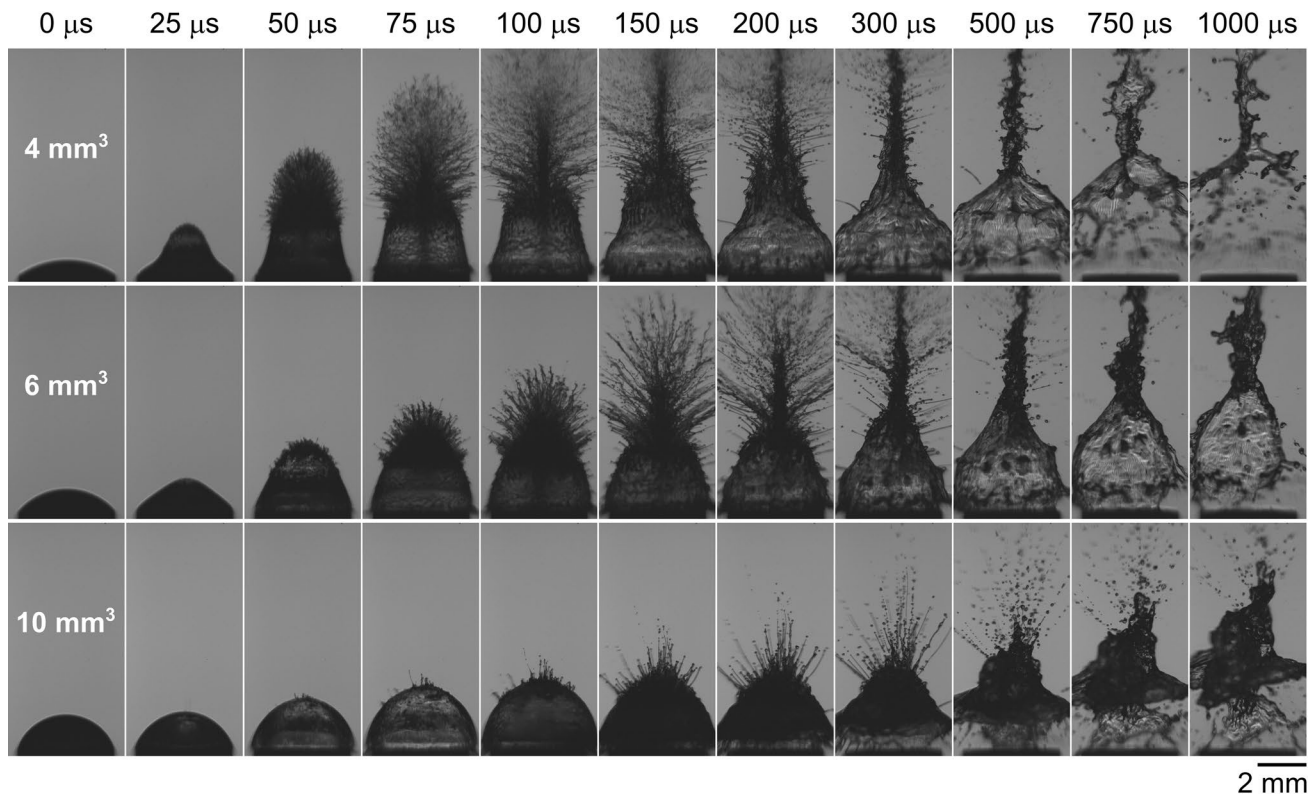


Fig. 7 Evolution of water ejection from the flat geometry (F) surface with different volumes of water applied to the target surface. The surface is positioned in the focus of the laser beam, which irradiates

from the top. Pulse energy and exposure times equal 10.6 mJ and 250 ns, respectively. Timescale on the top presents time interval after excitation-laser irradiation

layer. Similar phenomenon was observed by Nguyen et al. [38], who studied the effects of liquid depth h on dynamics of cavitation bubble by maximum radius R_{\max} . Their results clearly show that the liquid layer (with thickness $h \leq R_{\max}$) above the irradiated spot is pushed up by the laser-induced cavitation bubble that forms on the solid (target) surface. This effect depends on the dimensionless parameter $\xi = h/R_{\max}$ and is more apparent for $\xi < 1$; while it disappears, when the thickness of the water layer exceeds the bubble's radius ($\xi > 1$). As visible from Fig. S4 (Supplementary Material), the maximum bubble radius in our case for 10-mm-thick water layer equals $R_{\max} \approx 2$ mm, if the laser is focused on the target surface.

Figure 7 shows that the most disintegrated jet during the perforation of the liquid–air interface appears in case of the smallest water droplet ($V = 4 \text{ mm}^3$, $t = 25 \text{ } \mu\text{s}$), where the highest point of the liquid layer is approximately $h = 0.7$ mm above the solid surface, yielding $\xi \approx 0.35$. Thus, as visible from image acquired 1 ms after the excitation–laser irradiation, under this condition the water layer is most efficiently wrenched off the solid surface. The effect is much less pronounced for $V = 10 \text{ mm}^3$, where $h = 1.5$ mm leads to $\xi \approx 0.75$, which means that the final bubble is just slightly larger than the layer thickness. As visible from the results in Fig. 7, the parameter ξ plays a significant role in efficiency of the ejected water. Since the liquid, ablated from the target surface contributes into the rod propulsion, this parameter should influence also the propulsion efficiency.

3.3 The effect of the focal position

The effect of the focal position has also been investigated by moving the focusing lens of the excitation pulses with respect to the target surface (see Fig. 8a). Due to different refractive indices of water and air, lens displacement (in air) Δz does not correspond to an equal shift of the focal position inside the water droplet Δf [39]. Furthermore, the curvature

R of the water surface leads to lensing effects that additionally alter the irradiated fluence. As shown by Favre et al. [40], a convex water surface focuses the laser beam by acting as a spherical lens. The position of the laser-induced water breakdown is (in addition to the focal position) also dependent on purity of water, since the impurities can decrease the threshold fluence for ionization, promoting breakdown out of the focal spot [31]. A change in the focal position (with respect to the rod surface) inside the water droplet Δf can, therefore, be written as a function of Δz and R , as shown by Eq. (8). In case of a flat air–water interface, R goes to ∞ and Eq. (8) can be simplified to a linear relation to Δz , where the scaling factor depends on the ratio between the refractive indices of water and air (Eq. 9):

$$\Delta f = \Psi(\Delta z, R), \quad (8)$$

$$\Delta f = \Psi(\Delta z, \infty) = \Delta z \frac{n_{\text{water}}}{n_{\text{air}}}. \quad (9)$$

The influence of the lens displacement on the position of the laser-induced breakdown was determined by shadow-graphic observation (Figs. 8b, 9a; Figs. S1–S10 in Supplementary Material). For this purpose, the aluminum rod with flat geometry (F) was submerged into water approximately 10 mm below the flat (free) water surface and irradiated with laser pulses of $E_p = 10.6$ mJ. Different focal positions were achieved by displacing the focusing lens with respect to the irradiated target surface in the range from $\Delta z = -5.0$ mm (inside the solid surface) to $\Delta z = +3.0$ mm (towards the laser).

As visible from Fig. 8b, moving the lens away from the target surface ($\Delta z > 0$) positions the focal spot above the solid surface and promotes the breakdown of (bulk) water instead of the (metallic) target. When the lens is moved for $\Delta z = +3.0$ mm (experiment in Fig. 8b, far right), the focal

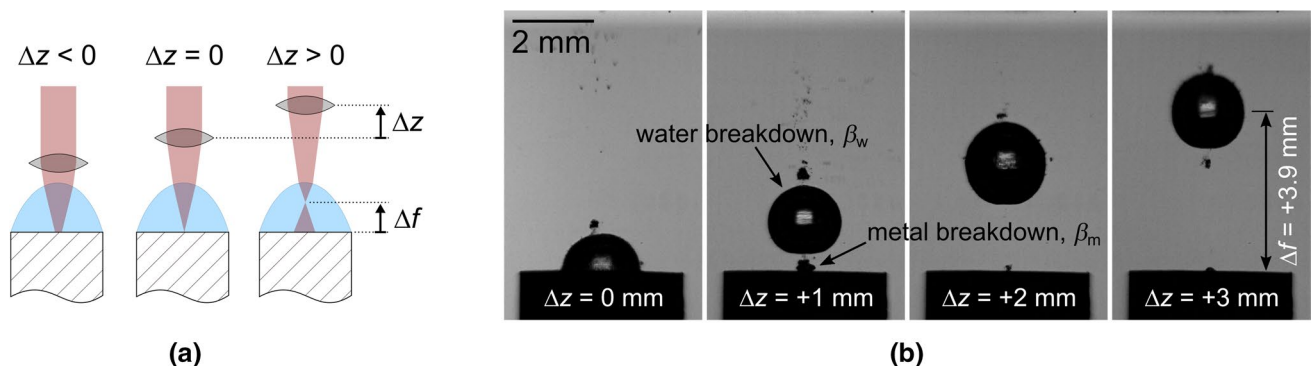


Fig. 8 **a** Definition of lens displacement Δz and change in focal position Δf . **b** Cavitation bubble approximately 50 μs after breakdown of water with focal position of the laser beam above the target surface ($\Delta z > 0$). Laser beam is incident from the top

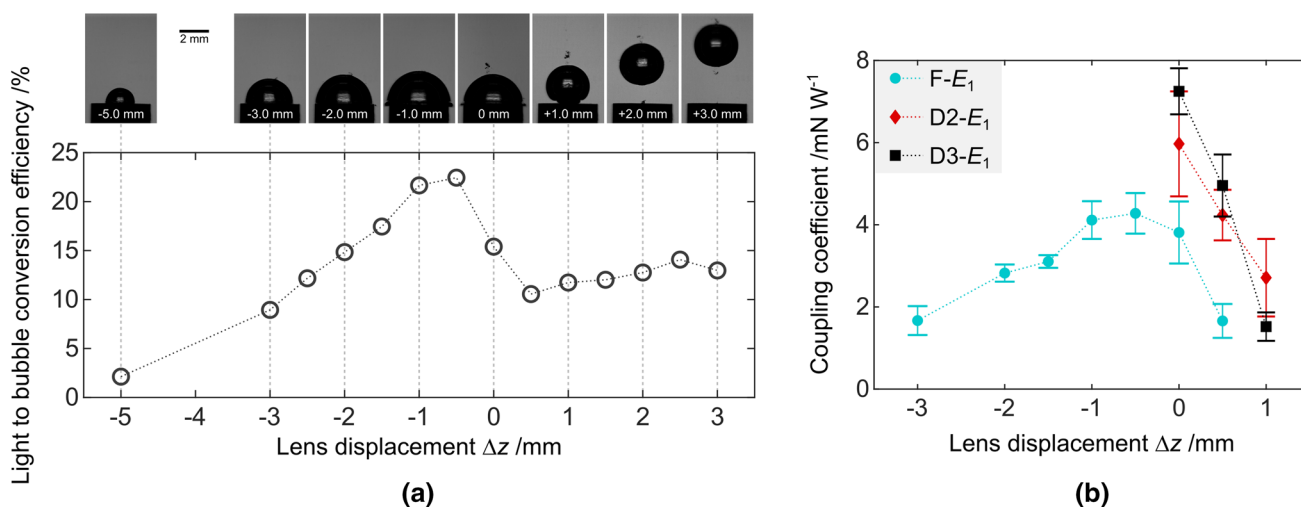


Fig. 9 a Conversion of light (pulse) energy into bubble energy for different lens displacements. On the top, corresponding images of bubble at its maximum size are shown. $E_p = 10.6$ mJ. **b** Coupling

coefficient for different confining geometries in dependence of lens displacement for pulse energy $E_1 = 10.6$ mJ and volume of water $V = 6$ mm³

position moves for $\Delta f = +3.9$ mm. This confirms the scaling factor for the refractive indices of water ($n_{\text{water}} = 1.3$) and air ($n_{\text{air}} = 1$) as predicted by the theoretical relation (Eq. 9). On contrarily, when the focus is placed at $z < 0$, the center of the laser-induced bubble always remains on the target surface (e.g., see Figs. S1–S4 in Supplementary Material), but the irradiated laser fluence on the solid surface decreases.

The results in Fig. 8b and Figs. S5–S10 (Supplementary Material) reveal that moving the focal spot towards the laser leads to the formation of two separated cavitation bubbles—one in the focal position (in bulk water) and another located on the target (metallic) surface. The latter occurs, since metal has lower threshold for the optical breakdown as (pure) water. If the focal position is not too far from the metallic surface, this leads to formation of plasma on the target surface in the very beginning of the laser pulse, when the fluence in the focal spot is still below the threshold for water breakdown. After the fluence exceeds the threshold for water breakdown, the plasma forms also in the focal spot of the beam. Absorption of the pulse energy by this plasma decreases the amount of the laser radiation reaching areas beyond the focal point [36], therefore ceasing ablation of the target surface. This effect is known as plasma shielding [41].

From the obtained shadowgraphs, the mechanical energy of the cavitation bubble E_B can be estimated as [42]:

$$E_B = p_\infty V_{\text{max}}, \tag{10}$$

where V_{max} stands for the bubble volume at its maximum size, while $p_\infty = 10^5$ Pa equals the hydrostatic pressure.

Volume of the cavitation bubble was determined by image processing, presuming axial symmetry of the bubble,

similarly as described in Ref. [43]. Results, presented in Fig. 9a, show the measured conversion efficiency of light (laser pulse) energy into bubble energy E_B/E_p for different lens displacements. Interestingly, maximum conversion efficiency ($\sim 22\%$) is not achieved when the focal spot is positioned exactly on the target surface, but rather slightly below it ($\Delta z = -0.5$ mm). This could be explained by reduced plasma shielding above the target surface due to lower fluence in the irradiated spot. As has already been shown for the same laser system [44], the plasma in bulk water is approximately 300- μm long. Greater lens displacements towards the surface further reduce the fluence, leading to decreased energy-conversion efficiency.

As visible from Fig. 9a, the light-to-bubble conversion efficiency has three different regimes. The first regime is at $\Delta z > +0.5$ mm. Here, the conversion efficiency does not depend on the focal position (within the measurement uncertainty) and for our laser fluences equals between 10 and 15%. The efficiency increases (up to 22%), when the focal position approaches the target surface and decreases, if the focal position is moved further inside the metallic material. This can be most conveniently explained by introducing the normalized laser-pulse fluence [36]:

$$\beta = \frac{F}{F_{\text{th}}}. \tag{11}$$

In Eq. (11), F_{th} stands for the fluence threshold for breakdown. At other parameters such as pulse duration remaining constant, higher β yields higher bubble energies. As the metals contain free electrons, their threshold fluence for breakdown is lower than that of water, leading to $\beta_m > \beta_w$, where

indices m and w stand for metal and water, respectively. Due to this reason, the bubbles with larger maximal volume are developed, when the laser pulse is focused to the metallic surface as in the bulk water. However, if the focus is moved further inside the solid, this decreases F in Eq. (11) and, consequently, also decreases energy-conversion efficiency [11, 12].

The results presented in Fig. 9b show that the coupling coefficient is decreased when the focal position of the lens is moved away from the target surface. For $\Delta z < 0$ the trend

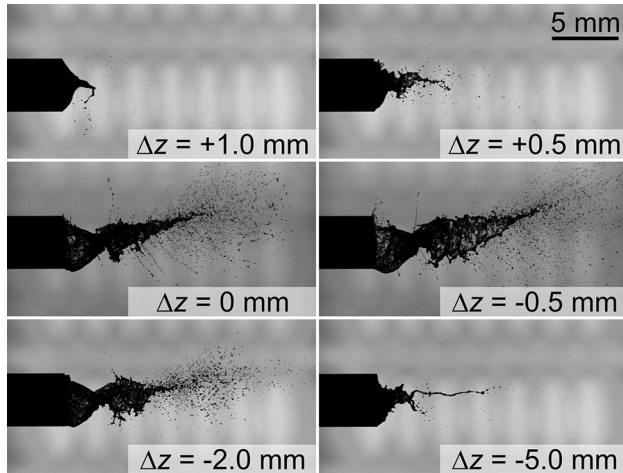


Fig. 10 Ejection of water from flat surface (F) at different lens displacements 400 μ s after the irradiation. Laser beam is incident from the right

corresponds well with the light-to-bubble conversion efficiency, shown in Fig. 9a. When this efficiency increases, larger bubble develops which significantly affects the water ablation as can be seen from Fig. 10 and Figs. S11–S17 in Supplementary Material. When the largest bubble is developed ($\Delta z = -0.5$ mm), all water is efficiently removed from the surface within the first millisecond after the excitation pulse (e.g., see Fig. S16 in Supplementary Material), since $\xi \approx 0.4$. On contrarily, as clearly visible by the sequence of images shown in Fig. S11 (Supplementary Material) at $\Delta z = -5.0$ mm, the small bubble ($R_{\max} \approx 1.0$ mm) is not able to remove the water layer ($h \approx 1$ mm) from the target surface. As shown by the results in Fig. 7, this happens since $\xi \approx 1$.

On contrarily, the decrease of the coupling coefficient for $\Delta z > 0$ is explained by the movement of the bubble's position. As shown by Figs. 8b and 9a, in this case, the bubble is moved away from the surface towards the gas–liquid interface. As clearly visible from Fig. 10 and Figs. S18–S21, the initiation of the bubble near the liquid–gas interface results in only partially ablated water, when the flat geometry is used.

Similar trend of the coupling coefficient as a function of the focal position is observed also for D2 and D3 geometries. A typical sequence of images acquired during the water ejection in case of the geometry D3 is shown in Fig. 11. Similar to experiments with different water volumes, a T-shape jet of the ejected water yields highest coupling coefficients. This occurs when the target surface is in the focal position. Albeit the maximum velocity of water is higher when Δz

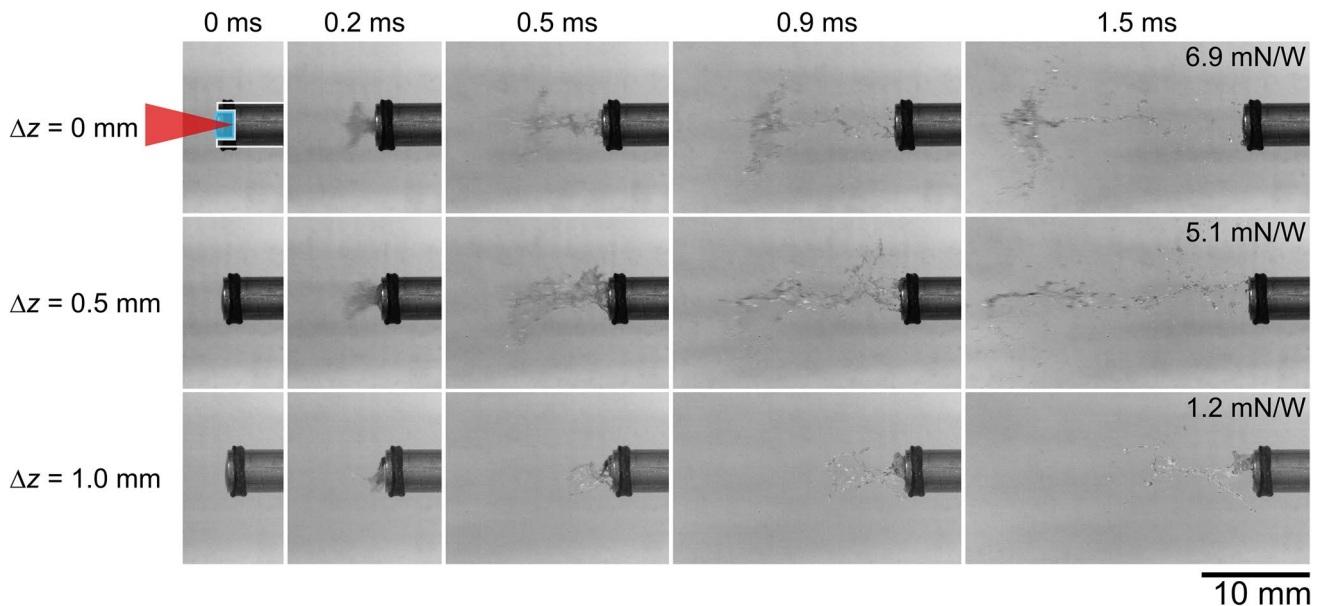


Fig. 11 The ejection of water at different lens displacements for the rod geometry D3. Pulse energy and volume of water equal 10.6 mJ and 6 mm³, respectively. The coupling coefficient is noted in the top right corner

equals +0.5 mm, the center of mass lags behind compared to ablation in focus, leading to smaller total momentum of the ejected water. At highest distance from focus, the laser-induced cavitation bubble is, similarly as in case of the flat geometry, not anymore able to overcome the surface tension and eject all the confining water. In addition to lower jet velocity, the decrease in the ejected mass further leads to substantially lower propulsion effects.

4 Conclusions

Coupling coefficient and energy-conversion efficiency in the ablative laser propulsion have been investigated with respect to parameters including pulse energy, distance of the target surface of the propelled rod from focus, and volume of water confined by different geometries. Our results show that the confinement by liquid (a free boundary) and surface geometry (a solid boundary in forms of cavity) substantially increases the propulsion effects by directing the ejected flow of the liquid.

Results reveal that maximum propulsion efficiency is achieved when the confining water is ejected in a compact form with most of the mass following the same trajectory with the same velocity and just little dispersion in the lateral directions. In such case, the jet of water resembles a shape of the letter T. The exact micro-dynamics that leads to the T shape of the ejected water jet should be further investigated. However, from the presented results, it follows that the propelled rod carries below 0.5% of the final mechanical energy; while, the rest of this energy is transferred into the kinetic energy of the ablated water.

The high-speed shadowgraphs of the ejected water additionally reveal that the water layer thickness significantly affects the efficiency of the water ejection. Additionally, moving the target surface away from the focal position also influences the propulsion efficiency. When the focus is moved inside the solid target, the coupling coefficient decreases due to decreased light-pulse-to-bubble conversion efficiency resulting in smaller cavitation bubbles. If the focus is moved outside the solid surface (i.e., towards the gas–liquid interface), lower propulsion efficiency is a consequence of the bubble center movement towards the gas–liquid interface. In this case, the bubble is not able to efficiently eject all the water from the solid target.

Acknowledgements The authors acknowledge the financial support from the Slovenian Research Agency (research core Funding No. P2-0392 and Project No. J2-1741). The authors are also thankful to Dr. Matej Hočevar from the Institute of metals and technology, Slovenia for his help with the 3D optical microscope characterization.

References

1. T. Požar, A. Babnik, J. Možina, *Opt. Express* **23**, 7978 (2015)
2. C. Phipps, M. Birkan, W. Bohn, H.-A. Eckel, H. Horisawa, T. Lippert, M. Michaelis, Y. Rezunkov, A. Sasoh, W. Schall, S. Scharring, J. Sinko, *J. Propuls. Power* **26**, 609 (2010)
3. Y.K. Bae, *Phys. Proc.* **38**, 253 (2012)
4. S. Choi, T.-H. Han, A.B. Gojani, J.J. Yoh, *Appl. Phys. A* **98**, 147 (2009)
5. T.T.P. Nguyen, R. Tanabe-Yamagishi, Y. Ito, *Appl. Surf. Sci.* **470**, 250 (2019)
6. T.T.P. Nguyen, R. Tanabe, Y. Ito, *Appl. Phys. Lett.* **102**, 124103 (2013)
7. B. Han, Z.-H. Shen, J. Lu, X.-W. Ni, *Opt. Lasers Eng.* **48**, 950 (2010)
8. Z.Y. Zheng, J. Zhang, Y. Zhang, F. Liu, M. Chen, X. Lu, Y.T. Li, *Appl. Phys. A* **85**, 441 (2006)
9. Z. Zheng, J. Zhang, X. Lu, Z. Hao, X. Yuan, Z. Wang, Z. Wei, *Appl. Phys. A* **83**, 329 (2006)
10. C.R. Phipps, T.P. Turner, R.F. Harrison, G.W. York, W.Z. Osborne, G.K. Anderson, X.F. Corlis, L.C. Haynes, H.S. Steele, K.C. Spicochi, T.R. King, *J. Appl. Phys.* **64**, 1083 (1988)
11. P. Gregorčič, J. Zadavec, J. Možina, M. Jezeršek, *Appl. Phys. A* **117**, 353 (2014)
12. J. Diaci, J. Možina, *J. Phys. Paris IV* **4**, C7 (1994)
13. A. Kanitz, M.R. Kalus, E.L. Gurevich, A. Ostendorf, S. Barcikowski, D. Amans, *Plasma Sources Sci. Technol.* **28**, 103001 (2019)
14. D. Zhang, B. Gökce, S. Barcikowski, *Chem. Rev.* **117**, 3990 (2017)
15. C.L. Sajti, R. Sattari, B.N. Chichkov, S. Barcikowski, *J. Phys. Chem. C* **114**, 2421 (2010)
16. P. Serra, A. Piqué, *Adv. Mater. Technol.* **4**, 1800099 (2019)
17. A. Piqué, P. Serra, *Laser printing of functional materials: 3D microfabrication, electronics and biomedicine* (John Wiley & Sons, NJ, 2018)
18. P. Peyre, R. Fabbro, *Opt. Quantum Electron.* **27**, 1213 (1995)
19. C.S. Montross, T. Wei, L. Ye, G. Clark, Y.-W. Mai, *Int. J. Fatigue* **24**, 1021 (2002)
20. M. Tsuyama, N. Ehara, K. Yamashita, M. Heya, H. Nakano, *Appl. Phys. A* **124**, 250 (2018)
21. P. Gregorčič, N. Lukač, J. Možina, M. Jezeršek, *J. Biomed. Opt.* **21**, 015008 (2016)
22. G. Hawlina, B. Drnovšek-Olup, J. Možina, P. Gregorčič, *Appl. Phys. A* **122**, 118 (2016)
23. T. Požar, M. Halilovič, D. Horvat, R. Petkovšek, *Appl. Phys. A* **124**, 112 (2018)
24. C. Phipps, M. Birkan, W. Bohn, H.-A. Eckel, H. Horisawa, T. Lippert, M. Michaelis, Y. Rezunkov, A. Sasoh, W. Schall, *J. Propuls. Power* **26**, 609 (2010)
25. H. Yu, H. Li, Y. Wang, L. Cui, S. Liu, J. Yang, *Opt. Laser Technol.* **100**, 57 (2018)
26. T. Yabe, Y. Ohzono, T. Ohkubo, C. Baasandash, M. Yamaguchi, T. Oku, K. Taniguchi, S. Miyazaki, R. Akoh, Y. Ogata, B. Rosenberg, M. Yoshida, *AIP Conf. Proc.* **702**, 503 (2004)
27. T. Yabe, *AIP Conf. Proc.* **766**, 567 (2005)
28. T. Yabe, C. Phipps, M. Yamaguchi, R. Nakagawa, K. Aoki, H. Mine, Y. Ogata, C. Baasandash, M. Nakagawa, E. Fujiwara, *Appl. Phys. Lett.* **80**, 4318 (2002)
29. T. Yabe, Y. Ogata, M. Yamaguchi, R. Nakagawa, K. Aoki, *Int. Congr. Appl. Lasers Electro-Opt.* **2002**, 161511 (2002)
30. P.K. Kennedy, *IEEE J. Quantum Elect.* **31**, 2241 (1995)
31. J. Noack, D.X. Hammer, G.D. Noojin, B.A. Rockwell, A. Vogel, *J. Appl. Phys.* **83**, 7488 (1998)
32. P. Gregorčič, J. Možina, G. Močnik, *Appl. Phys. A* **93**, 901 (2008)

33. P. Gregorčič, R. Petkovšek, J. Možina, *J. Appl. Phys.* **102**, 094904 (2007)
34. T. Požar, P. Gregorčič, J. Možina, *Opt. Express* **17**, 22906 (2009)
35. G.M. Hale, M.R. Querry, *Appl. Opt.* **12**, 555 (1973)
36. F. Docchio, P. Regondi, M.R.C. Capon, J. Mellerio, *Appl. Opt.* **27**, 3661 (1988)
37. A. Vogel, S. Busch, U. Parlitz, *J. Acoust. Soc. Am.* **100**, 148 (1996)
38. T.T. Nguyen, R. Tanabe-Yamagishi, Y. Ito, *Opt. Laser Eng.* **126**, 105937 (2020).
39. A. Menéndez-Manjón, P. Wagener, S. Barcikowski, *J. Phys. Chem. C* **115**, 5108 (2011)
40. C. Favre, V. Boutou, S.C. Hill, W. Zimmer, M. Krenz, H. Lambrecht, J. Yu, R.K. Chang, L. Woeste, J.-P. Wolf, *Phys. Rev. Lett.* **89**, 035002 (2002)
41. J.G. Fujimoto, W.Z. Lin, E.P. Ippen, C.A. Puliafito, R.F. Steinert, *Investig. Ophthalmol. Vis. Sci.* **26**, 1771 (1985)
42. R. Petkovšek, P. Gregorčič, *J. Appl. Phys.* **102**, 044909 (2007)
43. P. Gregorčič, M. Jezeršek, J. Možina, *J. Biomed. Opt.* **17**, 075006 (2012)
44. R. Petkovšek, P. Gregorčič, J. Možina, *Meas. Sci. Technol.* **18**, 2972 (2007)

Publisher's Note Springer Nature remains neutral with regard to jurisdictional claims in published maps and institutional affiliations.

Supplementary Material

Applied Physics A: Materials Science & Processing

Propulsion effects after laser ablation in water, confined by different geometries

Matej Senegačnik, Matija Jezeršek, Peter Gregorčič*

Faculty of Mechanical Engineering, University of Ljubljana, Aškerčeva 6, 1000 Ljubljana, Slovenia

Corresponding author:

* *E-mail: peter.gregorcic@fs.uni-lj.si (Peter Gregorčič)*

Table of Contents

1 Evolution of a laser-induced cavitation bubble at different focal positions

- Figure S1.* Evolution of cavitation bubble at $\Delta z = -5.0$ mm (focal position above the metal surface).
- Figure S2.* Evolution of cavitation bubble at $\Delta z = -3.0$ mm (focal position above the metal surface).
- Figure S3.* Evolution of cavitation bubble at $\Delta z = -0.5$ mm (focal position above the metal surface).
- Figure S4.* Evolution of cavitation bubble at $\Delta z = 0$ mm (focal position above the metal surface).
- Figure S5.* Evolution of cavitation bubble at $\Delta z = +0.5$ mm (focal position above the metal surface).
- Figure S6.* Evolution of cavitation bubble at $\Delta z = +1.0$ mm (focal position above the metal surface).
- Figure S7.* Evolution of cavitation bubble at $\Delta z = +1.5$ mm (focal position above the metal surface).
- Figure S8.* Evolution of cavitation bubble at $\Delta z = +2.0$ mm (focal position above the metal surface).
- Figure S9.* Evolution of cavitation bubble at $\Delta z = +2.5$ mm (focal position above the metal surface).
- Figure S10.* Evolution of cavitation bubble at $\Delta z = +3.0$ mm (focal position above the metal surface).

2 Ejection of water on a flat target surface at different focal positions

- Figure S11.* Evolution of water ejection at $\Delta z = -5.0$ mm (focal position inside the metal surface).
- Figure S12.* Evolution of water ejection at $\Delta z = -3.0$ mm (focal position inside the metal surface).
- Figure S13.* Evolution of water ejection at $\Delta z = -2.0$ mm (focal position inside the metal surface).
- Figure S14.* Evolution of water ejection at $\Delta z = -1.5$ mm (focal position inside the metal surface).
- Figure S15.* Evolution of water ejection at $\Delta z = -1.0$ mm (focal position inside the metal surface).
- Figure S16.* Evolution of water ejection at $\Delta z = -0.5$ mm (focal position inside the metal surface).
- Figure S17.* Evolution of water ejection at $\Delta z = 0$ mm (focal position on the metal surface).
- Figure S18.* Evolution of water ejection at $\Delta z = +0.5$ mm (focal position outside the metal surface).
- Figure S19.* Evolution of water ejection within the first 1500 μs at $\Delta z = +0.5$ mm (focal position outside the metal surface).
- Figure S20.* Evolution of water ejection at $\Delta z = +1.0$ mm (focal position outside the metal surface).
- Figure S21.* Evolution of water ejection within the first 1500 μs at $\Delta z = +1.0$ mm (focal position outside the metal surface).

1 Evolution of a laser-induced cavitation bubble at different focal positions

The flat (F) surface was irradiated with 10.6 mJ laser pulses at different lens displacements Δz . The flat surface of the rod was submerged in water approximately 15 mm below the water surface. Here we present the time lapse images, obtained by ultrafast camera. Time in microseconds is shown on the top of each image.

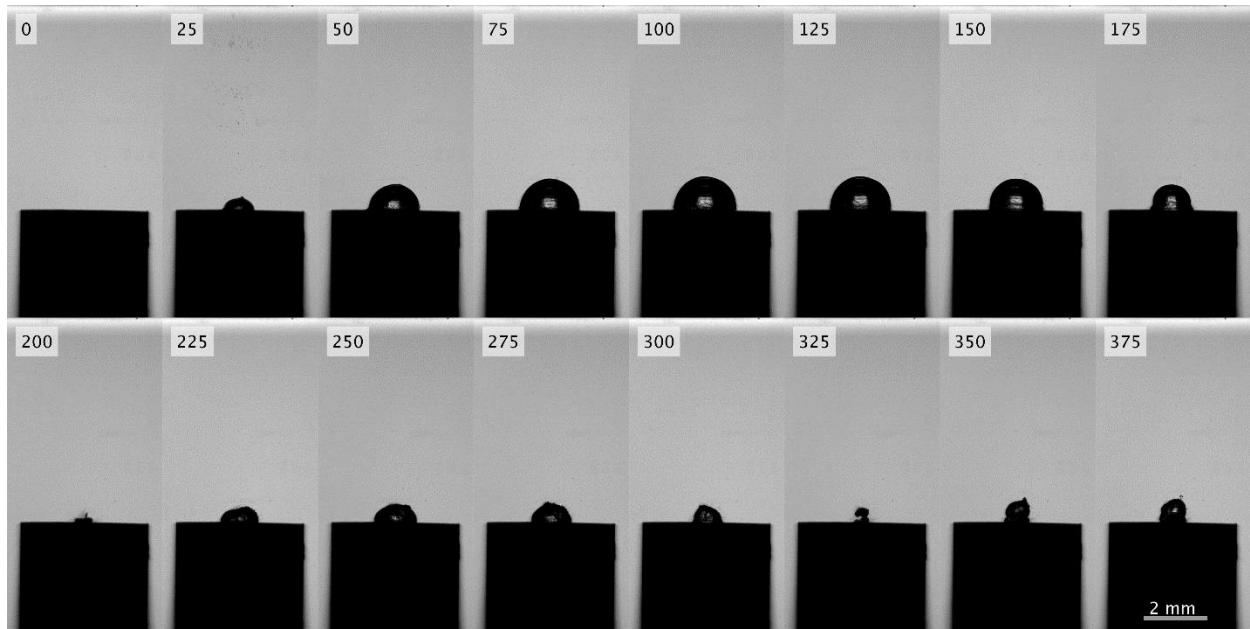


Figure S1. Evolution of cavitation bubble at $\Delta z = -5.0$ mm (focal position below the metal surface).

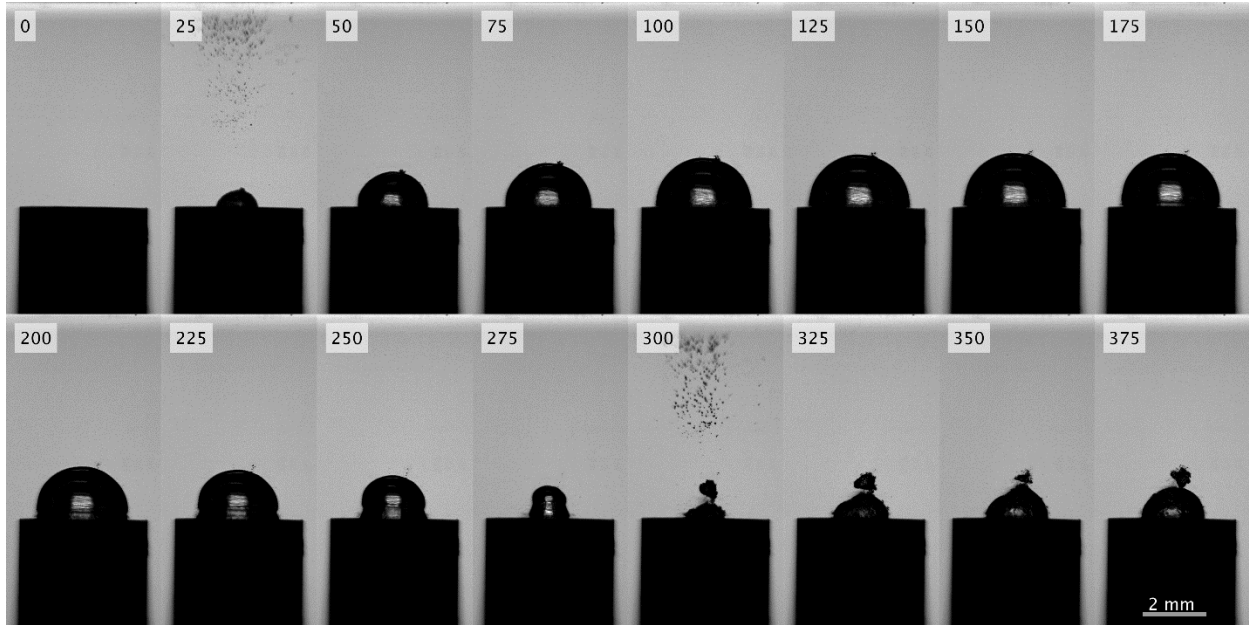


Figure S2. Evolution of cavitation bubble at $\Delta z = -3.0$ mm (focal position below the metal surface).

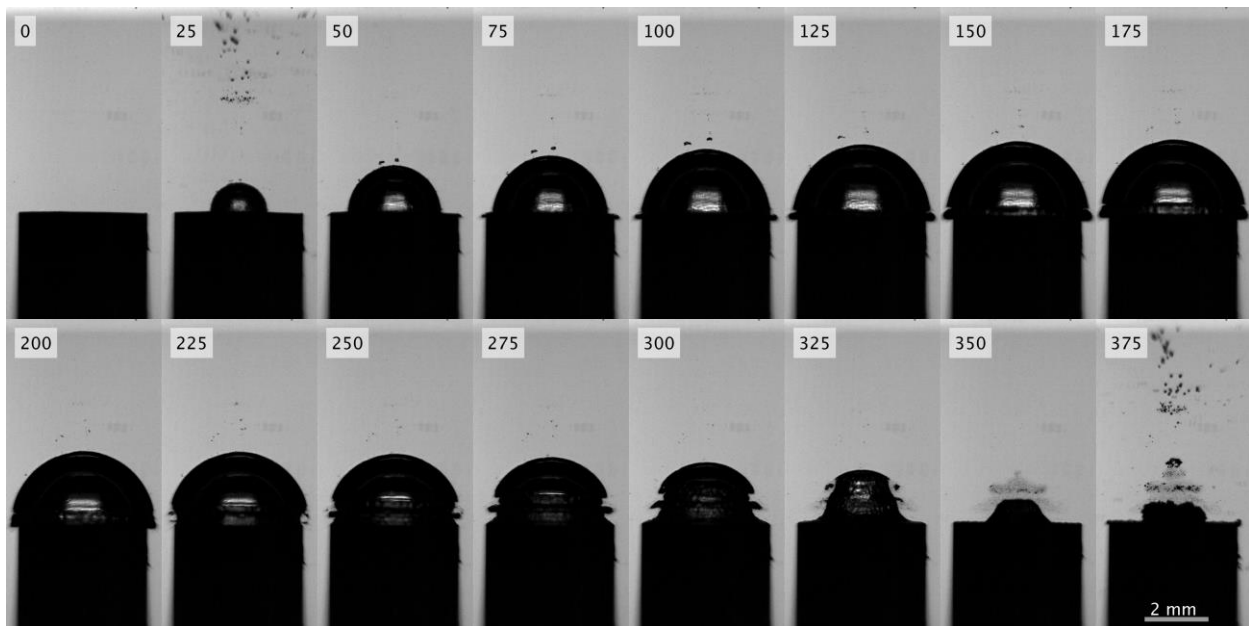


Figure S3. Evolution of cavitation bubble at $\Delta z = -0.5$ mm (focal position below the metal surface).

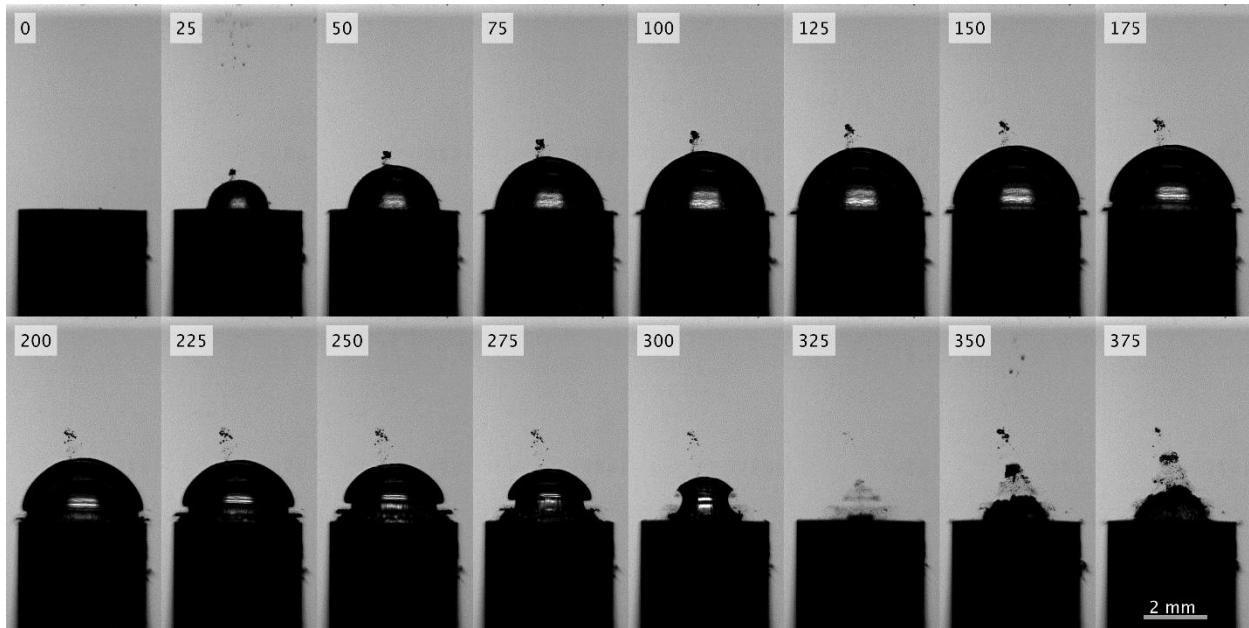


Figure S4. Evolution of cavitation bubble at $\Delta z = 0$ mm (focal position on the metal surface).

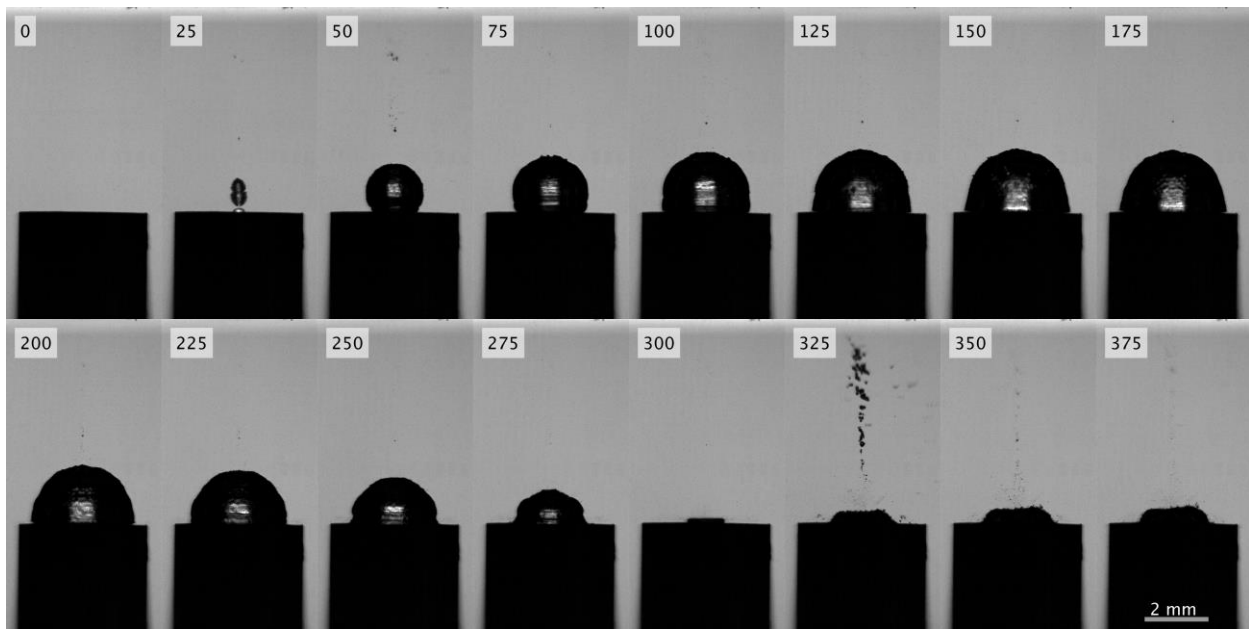


Figure S5. Evolution of cavitation bubble at $\Delta z = +0.5$ mm (focal position above the metal surface).

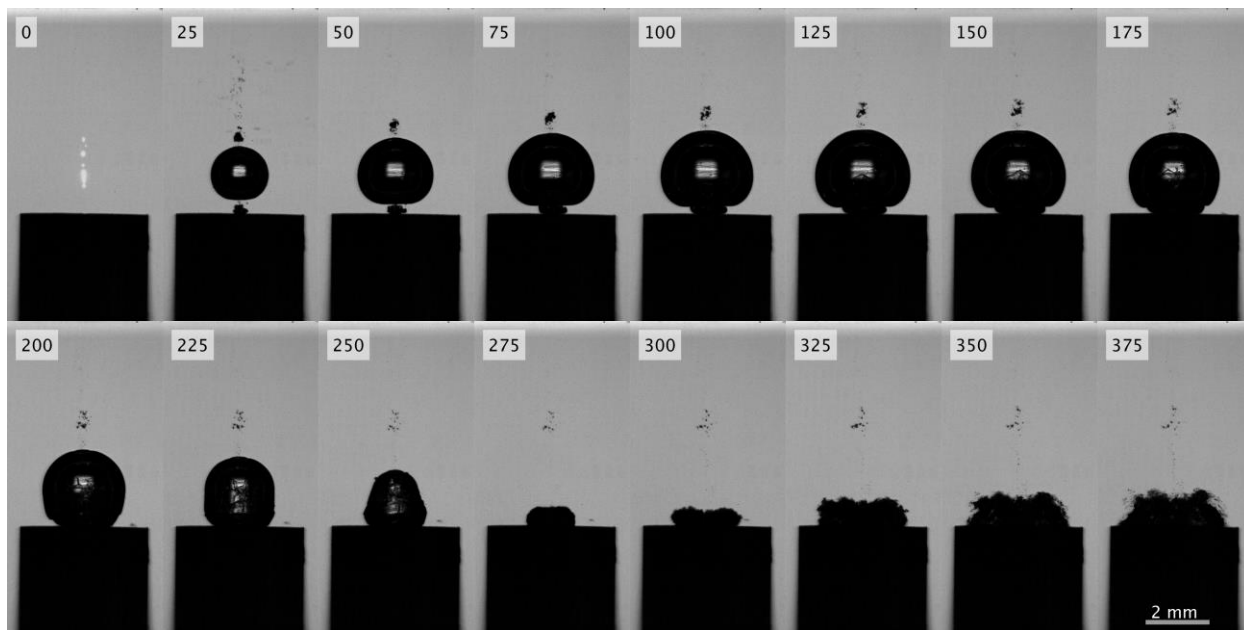


Figure S6. Evolution of cavitation bubble at $\Delta z = +1.0$ mm (focal position above the metal surface).

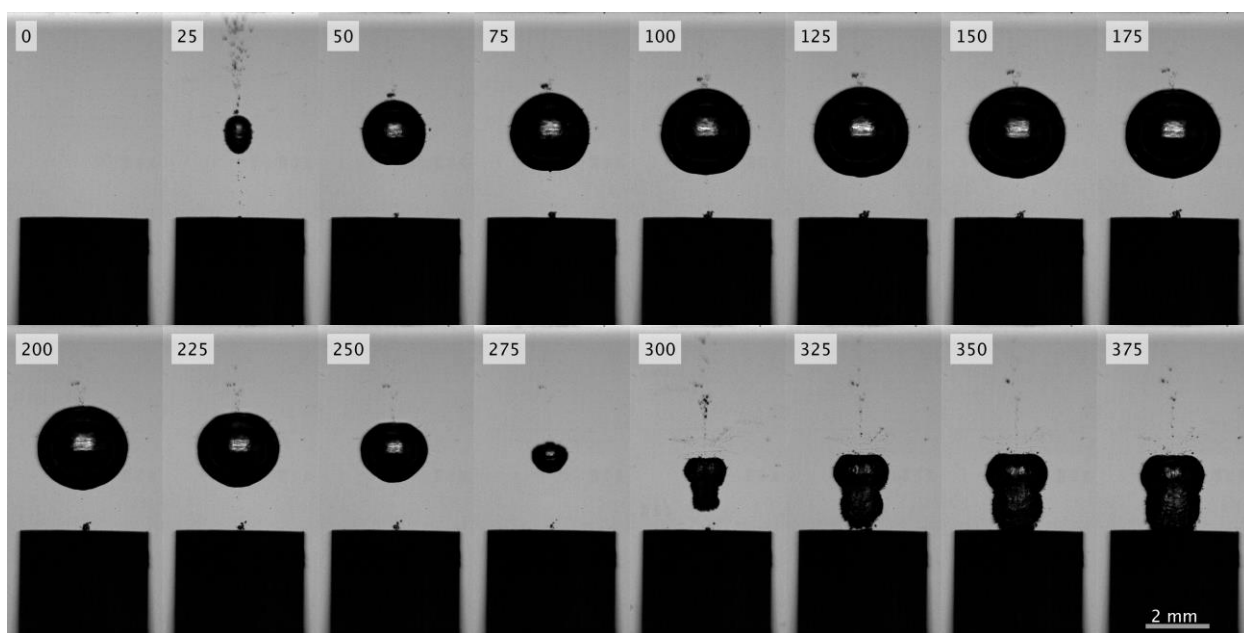


Figure S7. Evolution of cavitation bubble at $\Delta z = +1.5$ mm (focal position above the metal surface).

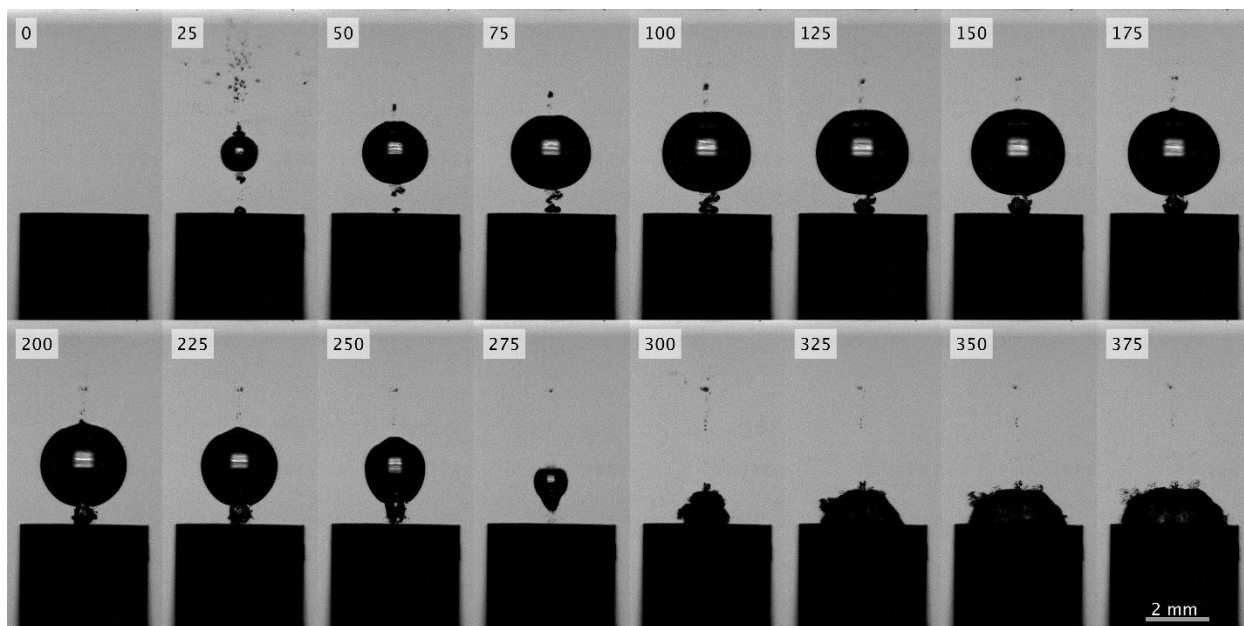


Figure S8. Evolution of cavitation bubble at $\Delta z = +2.0$ mm (focal position above the metal surface).

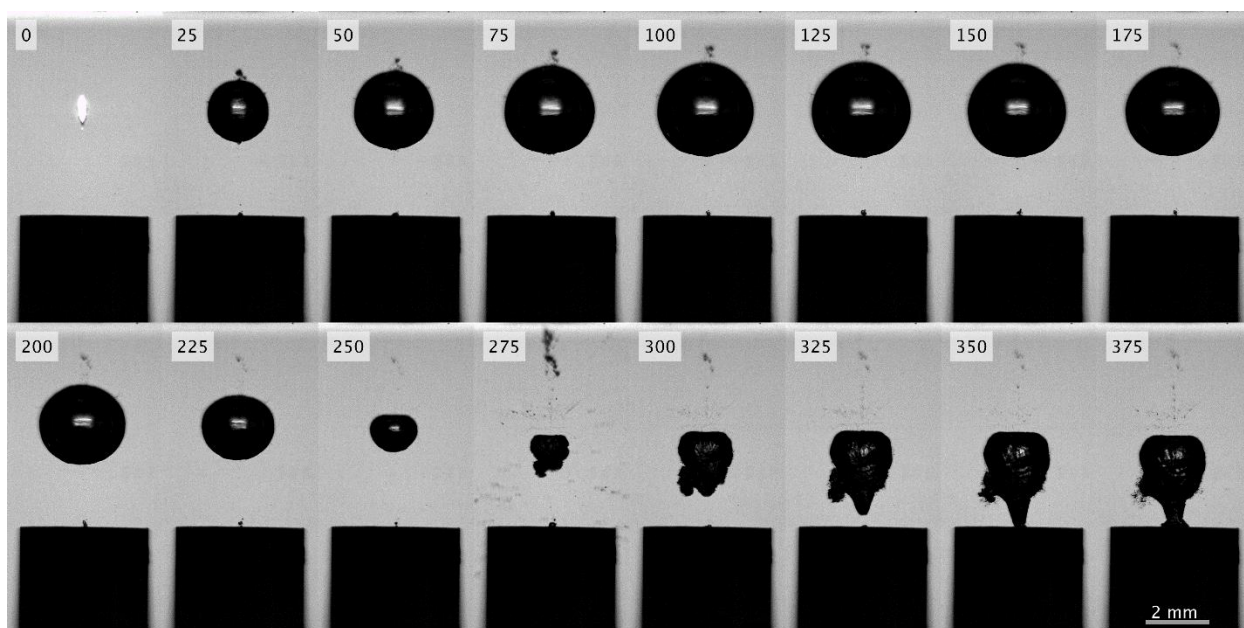


Figure S9. Evolution of cavitation bubble at $\Delta z = +2.5$ mm (focal position above the metal surface).

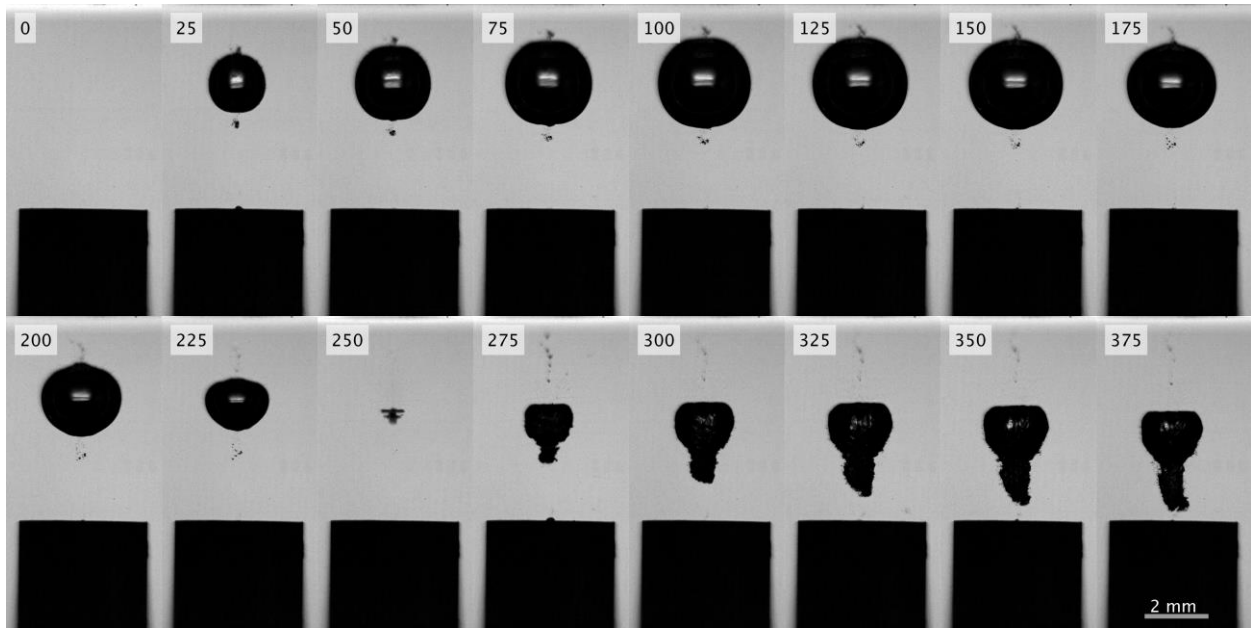


Figure S10. Evolution of cavitation bubble at $\Delta z = +3.0$ mm (focal position above the metal surface).

2 Ejection of water on a flat target surface at different focal positions

The flat (F) surface was irradiated with 10.6 mJ laser pulses at different lens displacements Δz . Here, we present the temporal evolution of the water jet. Timescale in microseconds is shown on the top of each image. Laser is incident from the right.

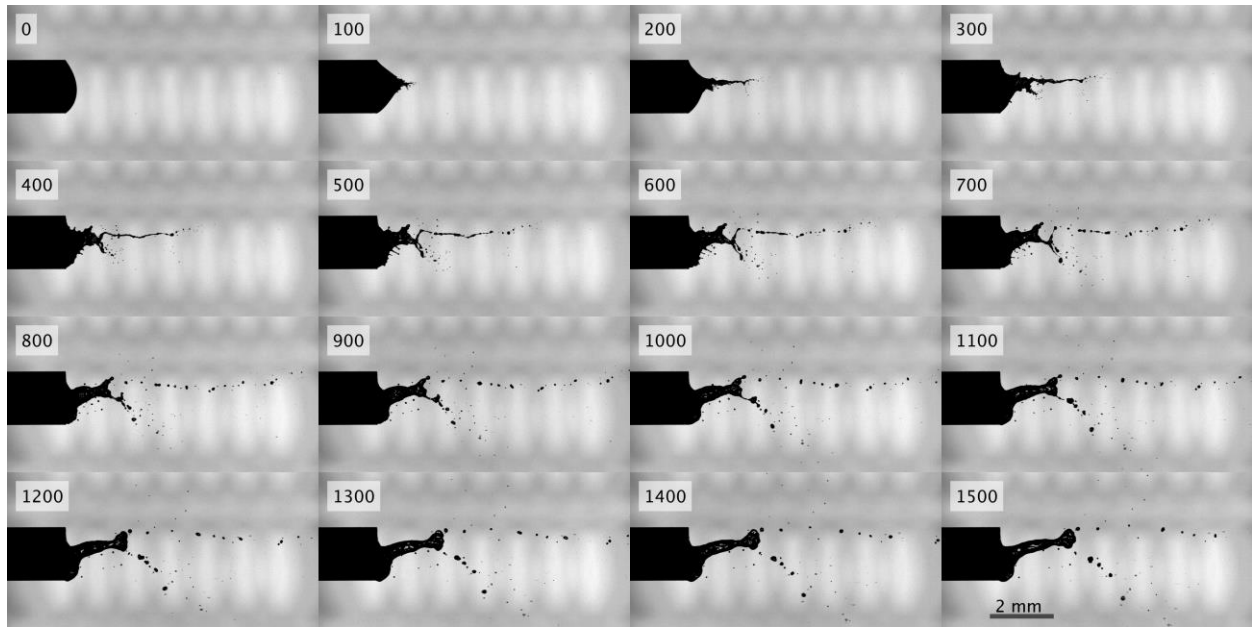


Figure S11. Evolution of water ejection at $\Delta z = -5.0$ mm (focal position inside the metal surface).

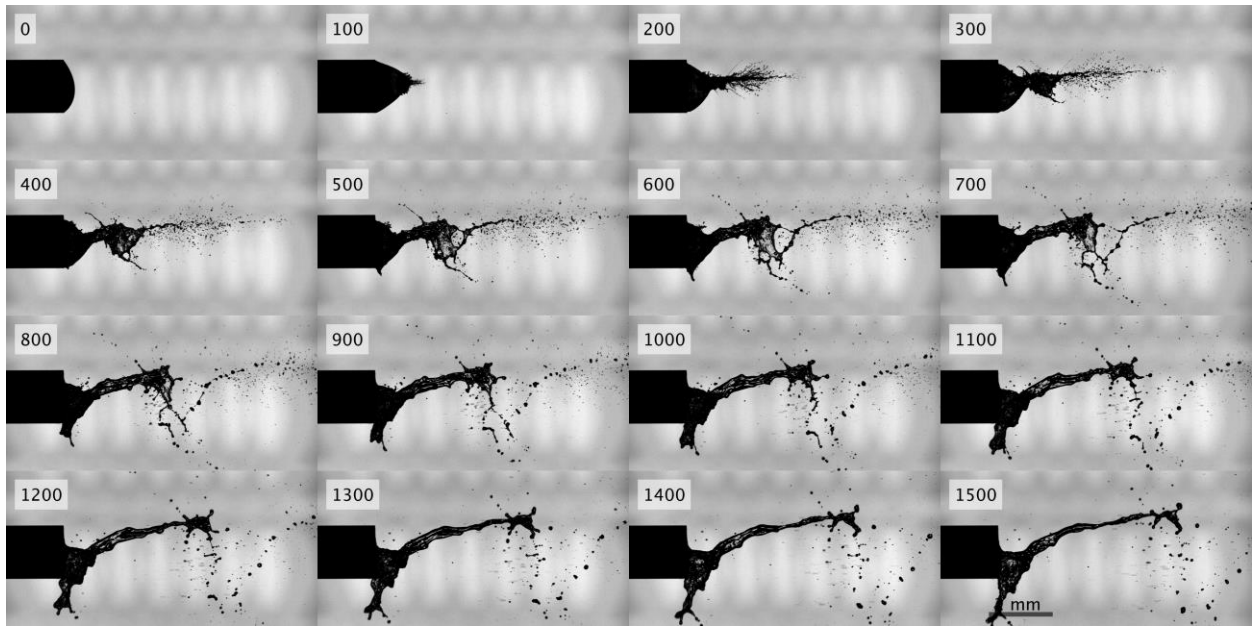


Figure S12. Evolution of water ejection at $\Delta z = -3.0$ mm (focal position inside the metal surface).

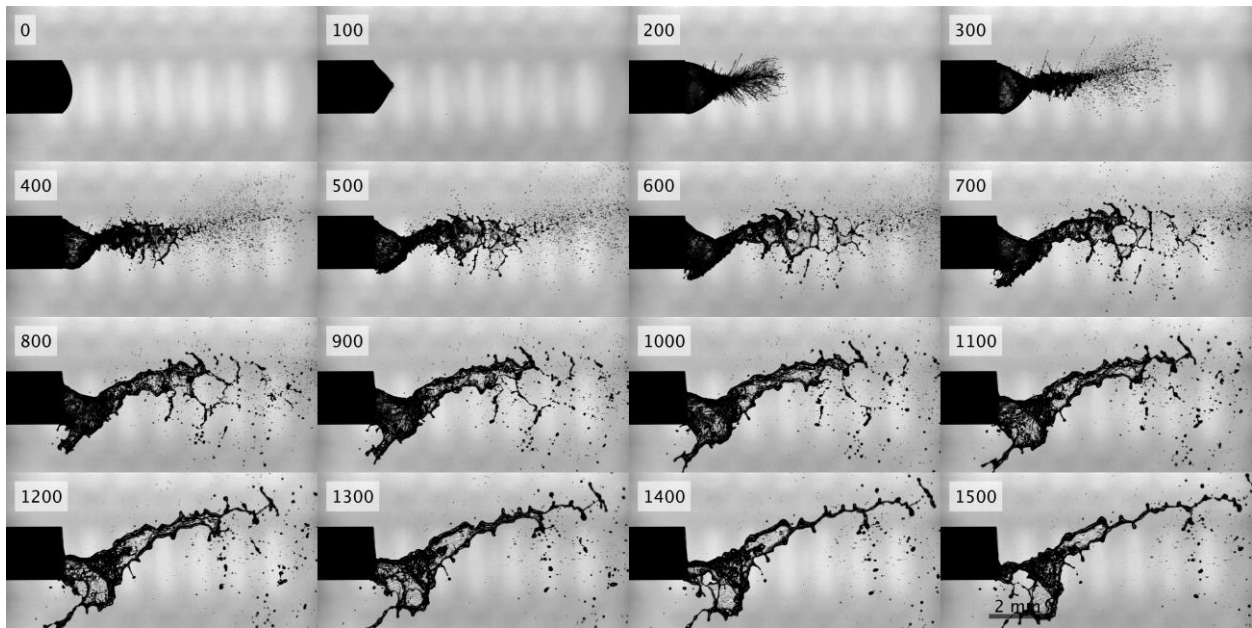


Figure S13. Evolution of water ejection at $\Delta z = -2.0$ mm (focal position inside the metal surface).

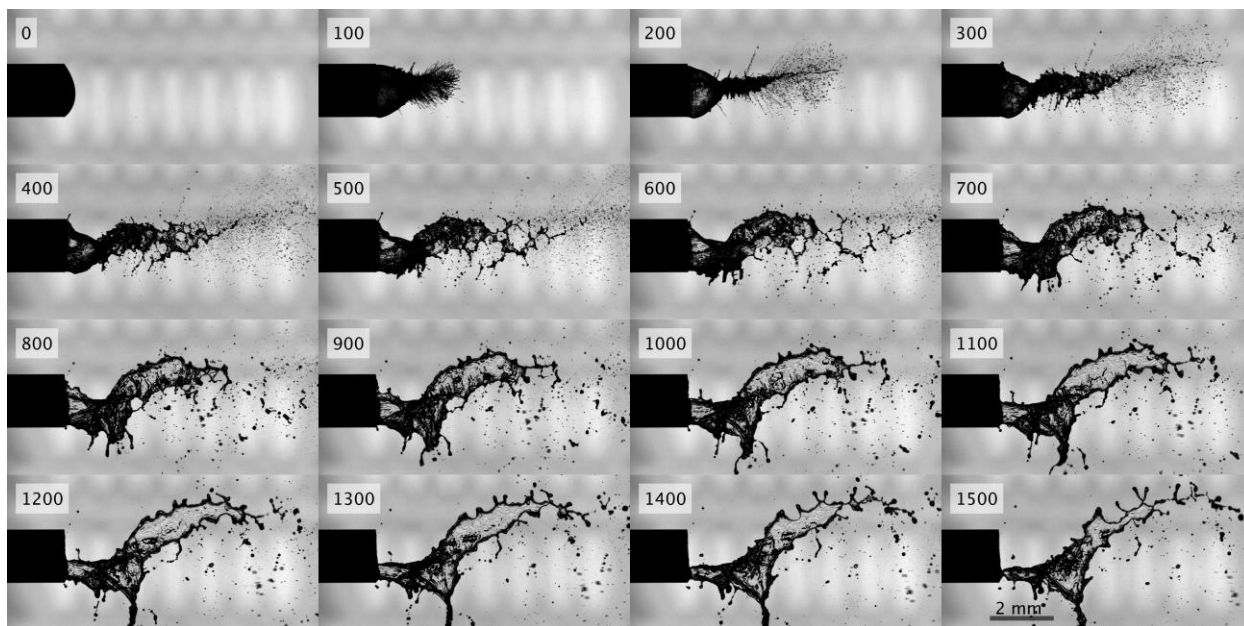


Figure S14. Evolution of water ejection at $\Delta z = -1.5$ mm (focal position inside the metal surface).

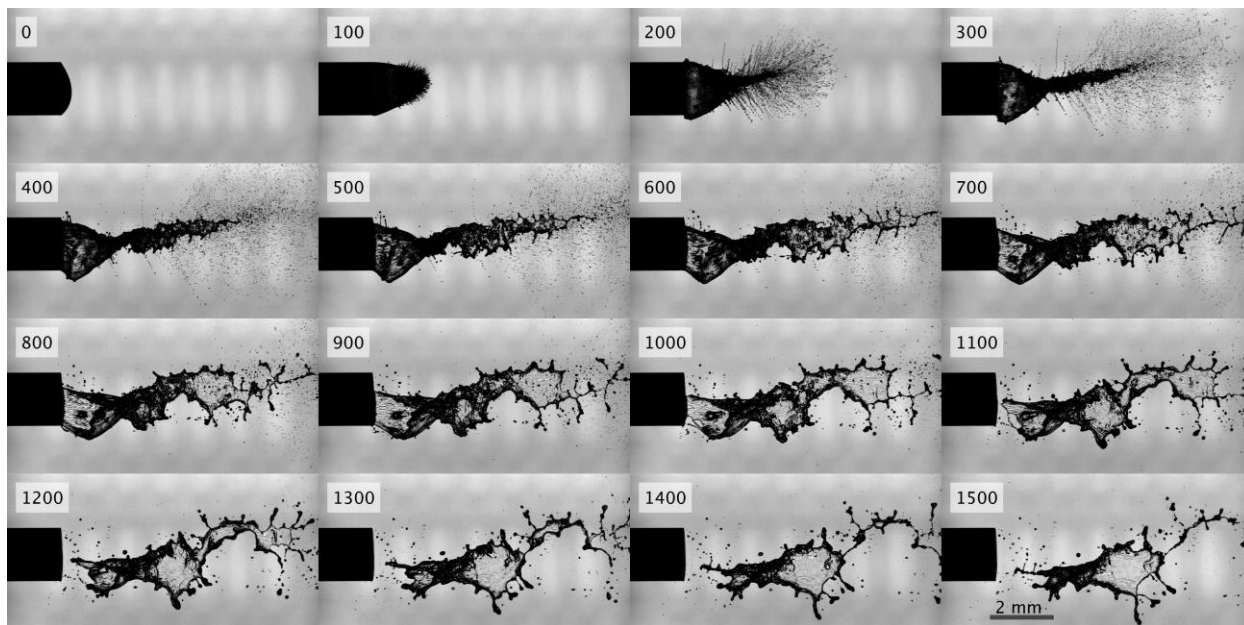


Figure S15. Evolution of water ejection at $\Delta z = -1.0$ mm (focal position inside the metal surface).

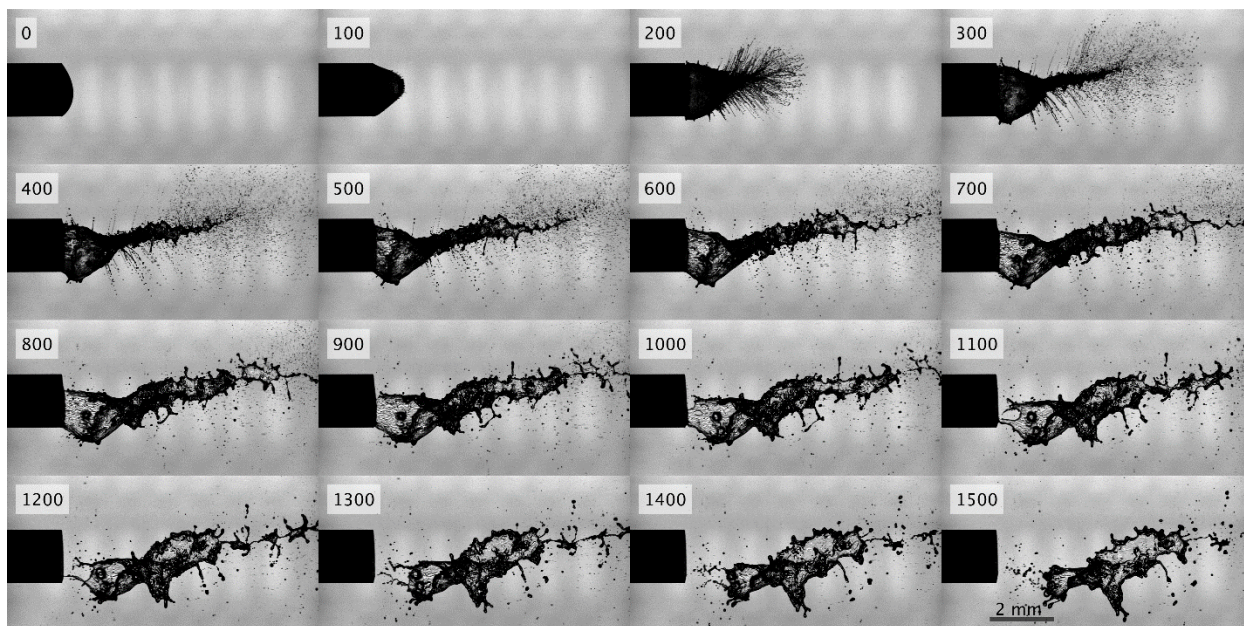


Figure S16. Evolution of water ejection at $\Delta z = -0.5$ mm (focal position inside the metal surface).

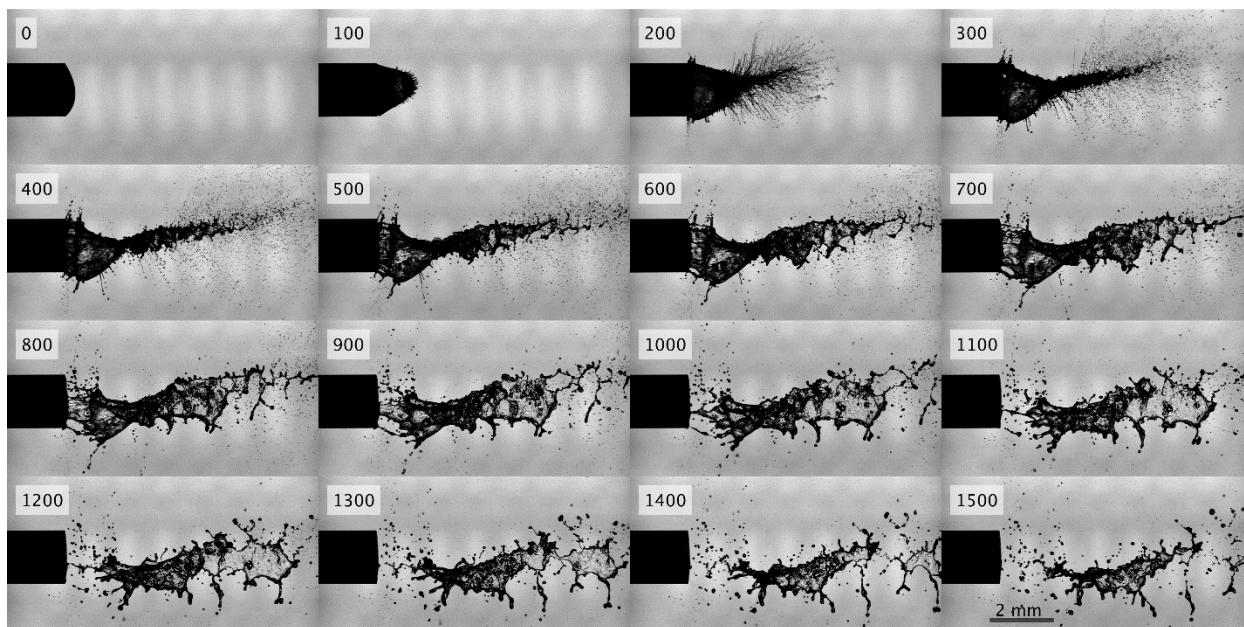


Figure S17. Evolution of water ejection at $\Delta z = 0$ mm (focal position on the metal surface).

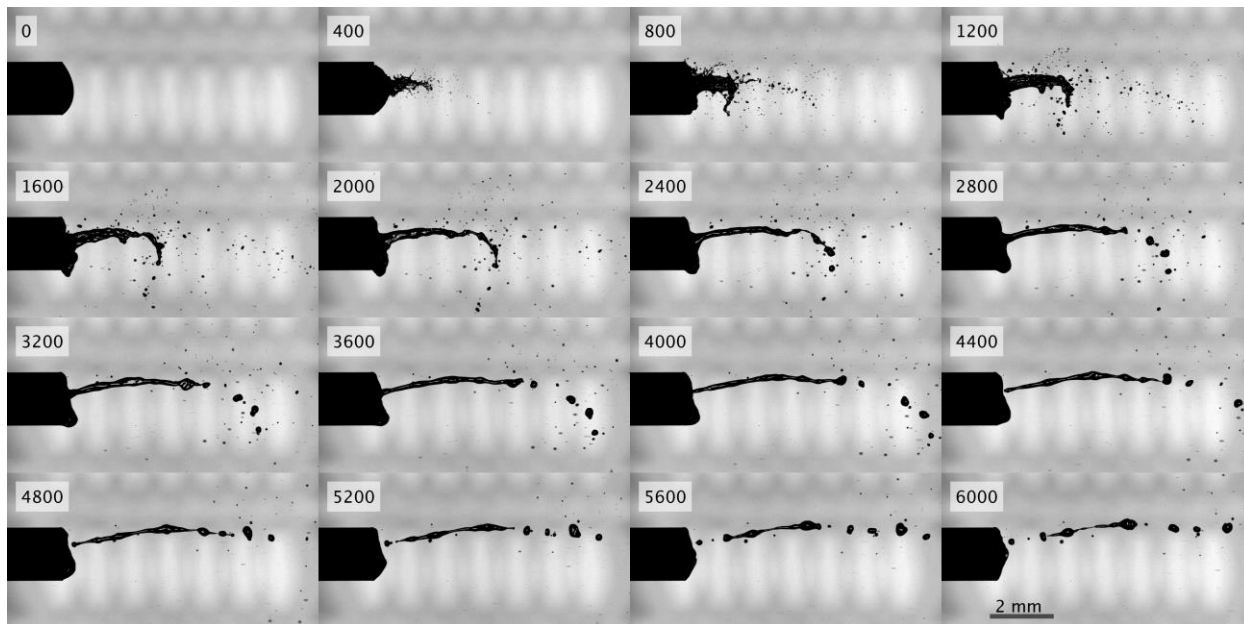


Figure S18. Evolution of water ejection at $\Delta z = +0.5$ mm (focal position outside the metal surface).

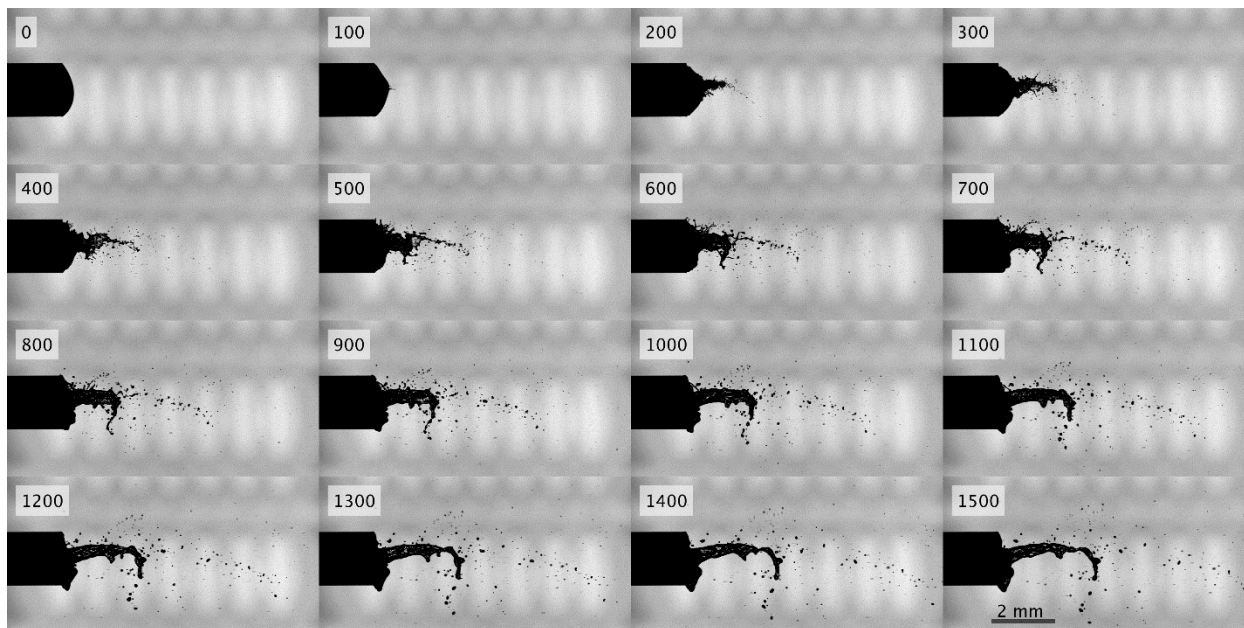


Figure S19. Evolution of water ejection within the first 1500 μ s at $\Delta z = +0.5$ mm (focal position outside the metal surface).

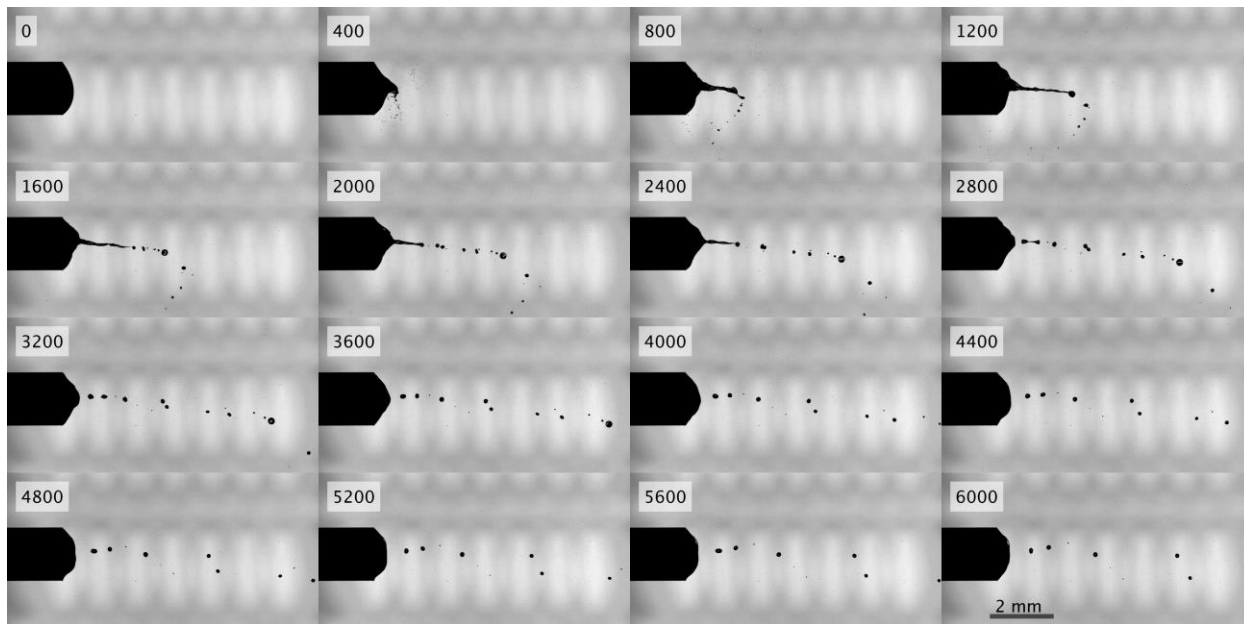


Figure S20. Evolution of water ejection at $\Delta z = +1.0$ mm (focal position outside the metal surface).

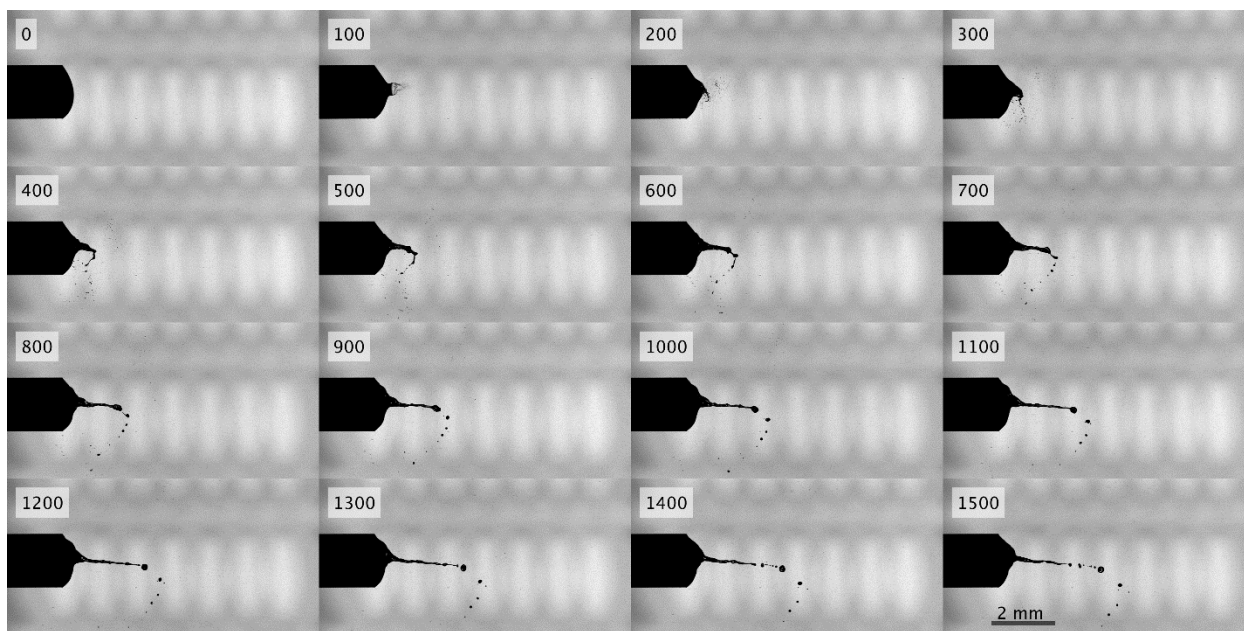


Figure S21. Evolution of water ejection within the first 1500 μs at $\Delta z = +1.0$ mm (focal position outside the metal surface).